On the Performance of Spatially Correlated Large Antenna Arrays for Millimeter-Wave Frequencies

Callum T. Neil, *Member, IEEE*, Adrian Garcia-Rodriguez, *Member, IEEE*, Peter J. Smith, *Fellow, IEEE*,
Pawel A. Dmochowski, Christos Masouros, *Senior Member, IEEE*, and Mansoor Shafi, *Fellow, IEEE*

Abstract—A spatially correlated large antenna array operating at millimeter-wave (mmWave) frequencies is considered. Based on a Saleh-Valenzuela channel model, closed-form expressions of the three-dimensional spatial correlation (SC) for wide, narrow and Von Mises power elevation spectra (PES) are analytically derived. The effects of the PES on the convergence to massive multiple-input-multiple-output (MIMO) properties is then illustrated by defining and deriving a diagonal dominance metric. Numerically, the effects of antenna element mutual coupling (MC) is shown on the effective SC, eigenvalue structure and mmWave user rate for different antenna topologies. It is concluded that although MC can significantly reduce SC for side-by-side dipole antenna elements, the change in antenna effective gain (and therefore signal-to-noise ratio) caused by MC becomes a dominating effect and ultimately determines the antenna array performance. The user rate of a mmWave system with hybrid beamforming (HBF), using an orthogonal matching pursuit (OMP) algorithm, is then shown for different antenna topologies with dipole and cross-polarized (x-pol) antenna elements. It is seen that even for small numbers of radio-frequency chains, the OMP algorithm works well relative to the fully digital case for channels with high SC, such as the x-pol antenna array.

I. INTRODUCTION

To cope with the demanding data rate specifications of 5G communication systems, novel technical solutions are being considered [1], [2]. Namely, the use of the wide bandwidths available at millimeter-wave (mmWave) frequency bands [3], dense deployment of cells [4] and massive multiple-input-multiple-output (MIMO) systems [5]. In this context, mmWave bands are suitable because they occupy regions of uncongested spectrum that enable large contiguous bandwidth carriers and the deployment of large-scale antenna arrays in smaller form factors [6], [7].

Recently, a number of papers have focused on characterizing radio wave propagation in the mmWave bands [7]–[14], where special emphasis has been placed on the development of statistical models based on measurement campaigns performed in urban environments. Some studies show that mmWave channels have significantly less multipath richness and a higher path loss (PL) than microwave channels [15]. It then follows that, in general, mmWave channels have an increased line-of-sight (LOS) propagation probability, since the cell radius must be reduced to maintain the same average received signal-to-noise ratio (SNR). Thus, the importance of both antenna directivity and array gains to overcome the increased propagation losses experienced at mmWave bands is highlighted.

A number of important metrics of MIMO communication systems, such as achievable rates and the number of independent data streams, are highly dependent on the SC characteristics, which are a function of both the wireless channel (e.g.,

number of scatterers) and the antenna array topology [16]–[21]. Due to the limited number of scattering clusters, as well as the narrow inter-cluster and intra-cluster angular spectra, mmWave communication channels have been shown to suffer from severe SC [8], [9], [12], [14], which diminishes the multiplexing and diversity gains attainable with large antenna arrays. This poses a challenge for mmWave transmission, since the resultant achievable data rates depend on the richness of the multipath channel [16], [19]–[21]. However, spatial channel sparsity can be simultaneously leveraged for reducing the number of radio frequency (RF) chains required for transmission via hybrid (analog and digital) beamforming (HBF) or beamspace strategies [22], [23]. Regardless, accurate models to quantify SC effects are needed to predict multiplexing gains and rates.

The analysis of SC has been the subject of a number of studies for both two-dimensional (2D) [20], [24] and three-dimensional (3D) [18], [25]–[27] scattering environments. The contribution in [24] assumes a narrow power azimuth spectrum (PAS) to derive the 2D SC of uniform linear array (ULA) and uniform circular antenna array topologies. Here, closed-form expressions of the SC are derived by taking the Fourier transform of the PAS. The work in [18] extends the methodology of [24] to a more realistic 3D propagation environment, deriving the SC of a uniform rectangular array (URA) and uniform cylindrical array (UCA), while exploring channel convergence properties of a massive MIMO system. Although quite general, the 3D SC analysis in [25]–[27] is non-closed-form, making it less straightforward to quickly draw conclusions regarding the influence of various SC mechanisms on performance. This limits their usefulness to some extent. Furthermore, the composite effect of large numbers of spatially correlated antennas on the performance (sum rate or eigenvalue properties) of a massive MIMO system is not considered in any of the aforementioned works. In this paper therefore, reasonable assumptions about the propagation environment are made such that closed-form expressions of the 3D SC can be derived and insights drawn. We also illustrate the combined effects of many spatially correlated antenna elements on the eigenvalue properties and rate of large scale antenna systems.

Mutual coupling (MC) between antenna elements has also been shown to be an influential factor in performance [28]–[31]. This effect can be critical in physically constrained scenarios, where a large number of antennas are packed in fixed physical structures such that inter-antenna spacings are shorter than half a wavelength, as studied in [17], [32]. Specifically, [32] shows a considerable decrease in the achievable rates of

microwave systems due to MC. Overall, the influence of both MC and array topology in the mmWave band still remains an open problem [13].

In this paper, the channel model is based on the well-known Saleh-Valenzuela (S-V) channel model [33]. The S-V style model has been the subject of a number studies (e.g., [34], [35]), and its capacity distribution accuracy has been validated, using MIMO system measurements, for various scenarios [36]–[38]. It thus forms the basis for 3rd Generation Partnership Project (3GPP) sub-6 GHz [39] and above 6 GHz [40] channel models. Due to its versatile structure, many mmWave measurement campaigns (e.g., [3], [8]–[10], [12], [14], [41], [42]) have adopted the S-V channel, where a few clusters and narrow angular spectra allow the modelling of sparse channels. Thus, the S-V model is typically used to analyse and evaluate techniques in mmWave channels, e.g., HBF algorithms [22], [43], [44].

Using the S-V channel model, we derive closed-form expressions characterizing the 3D SC of arbitrary antenna array configurations, thus providing insight into the design and performance of mmWave systems. In particular, we concentrate on the study of metrics conventionally employed for the analysis of systems with a large number of co-located antennas such as diagonal dominance, which we analytically characterize, and user rate with and without HBF. Additionally, we explore the system eigenvalue properties for a variety of antenna structures with the aim of determining their influence on the array spatial multiplexing gain [45]. Overall, the results derived in this paper allow us to characterize the impact of employing different array topologies in mmWave systems.

We summarize the contributions of this paper as follows:

1) We derive closed-form expressions for the 3D SC between any two antenna elements of a S-V channel model, for wide, narrow and Von Mises [46], [47] power elevation spectrum (PES). Note that while the analytical derivations of this paper are general and applicable to other systems applying the S-V model, such as wideband channels and standardized non-line-of-sight (NLOS) channel models developed by the 3GPP [39], [40], the conclusions and results of this paper are focused on mmWave systems.

2) We define a metric to measure the convergence of a user's channel to favourable propagation [48]: diagonal dominance[1]. We then derive its closed-form expressions for wide, narrow and Von Mises PES, and show how the PES and antenna topology impact the rate of convergence to massive MIMO properties.

3) Numerically, we examine the effects of MC on different antenna array topologies, by analysing the resultant SC against inter-element spacing, eigenvalue properties and user rates of a mmWave system. We demonstrate that while MC reduces SC for a wide range of inter-element distances and antenna configurations, the variation in

SNR becomes the dominant effect and can increase or decrease user rates depending on antenna spacing.

4) The user rate performance of a HBF mmWave system is shown for different antenna topologies with dipole[2] and cross-polarized (x-pol) antenna elements. It is seen that the relative difference between the HBF and fully digital rates reduces with increasing SC.

II. SYSTEM MODEL

A. Channel Model

We consider a single-cell DL system where an M antenna element BS serves users, with Q antennas each, in a single time/frequency resource. The SC of a wideband channel is left to future work. The $Q \times M$ DL channel matrix for an arbitrary user can be described as

$$\mathbf{H} = \sum_{c=1}^{C} \sum_{l=1}^{L} \frac{g_{c,l}}{\sqrt{L}} \mathbf{a}_{\text{RX}}\left(\phi_{c,l}^{\text{AOA}}, \theta_{c,l}^{\text{AOA}}\right) \mathbf{a}_{\text{TX}}^{\text{H}}\left(\phi_{c,l}^{\text{AOD}}, \theta_{c,l}^{\text{AOD}}\right), \quad (1)$$

where C is the number of scattering clusters, L is the number of propagation subpaths per cluster, $g_{c,l} \sim \mathcal{CN}\left(0, \gamma_c\right) \; \forall c, l$ is the independent and identically distributed (i.i.d.) complex small scale fading[3], where γ_c is the (normalized) power of cluster c. γ_c is calculated following the method in [8], which generates the *unnormalized* power of cluster c, γ_c', via $\gamma_c' = U_c^{r_\tau - 1} 10^{-0.1 X_c}$, where $U_c \sim \mathcal{U}[0,1]$, r_τ is a constant (equal to 2.8 and 3.0 for 28 GHz and 73 GHz channels, respectively) and $X_c \sim \mathcal{N}(0, \zeta^2)$ accounts for log-normal variations in the per-cluster power with variance ζ^2. Thus, the channel model in (1) is normalized. The angles $\phi_{c,l} \in [0, 2\pi) \; \forall c, l$ and $\theta_{c,l} \in [0, \pi) \; \forall c, l$ denote the azimuth and elevation angles, respectively, of subpath l in cluster c. $\mathbf{a}_{\text{TX}}(\phi_{c,l}^{\text{AOD}}, \theta_{c,l}^{\text{AOD}})$ and $\mathbf{a}_{\text{RX}}(\phi_{c,l}^{\text{AOA}}, \theta_{c,l}^{\text{AOA}})$ denote the $M \times 1$ transmitter (TX) and $Q \times 1$ receiver (RX) antenna array response vectors, given as

$$\mathbf{a}_{\text{TX}}(\phi_{c,l}^{\text{AOD}}, \theta_{c,l}^{\text{AOD}}) = \exp\left(j \frac{2\pi}{\lambda} \mathbf{W}_{\text{TX}} \mathbf{r}_{\text{TX}}(\phi_{c,l}^{\text{AOD}}, \theta_{c,l}^{\text{AOD}})\right), \quad (2)$$

$$\mathbf{a}_{\text{RX}}(\phi_{c,l}^{\text{AOA}}, \theta_{c,l}^{\text{AOA}}) = \exp\left(j \frac{2\pi}{\lambda} \mathbf{W}_{\text{RX}} \mathbf{r}_{\text{RX}}(\phi_{c,l}^{\text{AOA}}, \theta_{c,l}^{\text{AOA}})\right), \quad (3)$$

where λ is the wavelength of the carrier frequency, $\mathbf{W}_{\text{TX}}$ and $\mathbf{W}_{\text{RX}}$ are the $M \times 3$ and $Q \times 3$ location matrices of the TX and RX antenna elements in 3D Cartesian coordinates, respectively. $\mathbf{r}_{\text{TX}}(\phi_{c,l}^{\text{AOD}}, \theta_{c,l}^{\text{AOD}})$ and $\mathbf{r}_{\text{RX}}(\phi_{c,l}^{\text{AOA}}, \theta_{c,l}^{\text{AOA}})$ are the 3×1 spherical unit vectors of the TX and RX, respectively, where $\mathbf{r}(\phi, \theta) = [\sin(\theta)\cos(\phi), \sin(\theta)\sin(\phi), \cos(\theta)]^{\text{T}}$. It is assumed that the angles of departure (AODs) are independent of the angles of arrival (AOAs) and that the azimuth angles are independent of elevation angles. We define the subpath angles to be the sum of a central cluster angle, $\{\phi_{0,c}, \theta_{0,c}\}$, and an intra-cluster subpath offset, $\{\Delta\phi_{c,l}, \Delta\theta_{c,l}\}$, i.e., $\phi_{c,l} = \phi_{0,c} \pm \Delta\phi_{c,l} \; \forall c, l$ and $\theta_{c,l} = \theta_{0,c} \pm \Delta\theta_{c,l} \; \forall c, l$, for azimuth and elevation angles, respectively.

---

[1]Diagonal dominance has previously been defined for a single-antenna users uplink (UL) channel in [49]. In this paper, diagonal dominance is defined for a downlink (DL) channel where the user can have an arbitrary number of receive antenna elements.

[2]Throughout this paper, we use dipole to refer to a co-polarized (or vertically polarized [39]) half-wavelength antenna.

[3]In many S-V style channel models, such as those standardized by 3GPP [39], [40], the complex normal $g_{c,l} \sim \mathcal{CN}(0, \gamma_c)$ is simply replaced by $\sqrt{\gamma_c}\exp(j\psi_{c,l})$ where $\psi_{c,l} \sim \mathcal{U}[0, 2\pi]$. However, we have chosen to follow the channel model in [8], thus we use $g_{c,l}$.

B. Angular Power Spectra

It is common to define the angular variation in clustered channels via a PAS and power elevation spectrum (PES) for the central cluster angles and a second PAS/PES for the subpaths within a cluster. In this work, it is more convenient to define the global PAS and PES of all subpaths as $p_\Phi(\phi) = f_\Phi(\phi)$ and $p_\Theta(\theta) = f_\Theta(\theta)/\sin(\theta)$, respectively. Here, $f_\Phi(\phi)$ and $f_\Theta(\theta)$ denote the PDFs of the azimuth and elevation angles of an arbitrary subpath. We assume that the TX is omnidirectional with respect to the azimuth domain, as in mmWave measurement campaigns [8], [9], [12], [14], [41], [42], [50]. Because the azimuth central cluster AODs are $\mathcal{U}[0, 2\pi)$, it also follows that *on average* $p_\Phi(\phi_{c,l}^{\mathrm{AOD}}) \sim \mathcal{U}[0, 2\pi) \; \forall c, l$ since the addition of a random offset to a $\mathcal{U}[0, 2\pi)$ variable remains uniform over $[0, 2\pi)$. Similarly, we assume the central cluster AOAs are $\mathcal{U}[0, 2\pi)$ in azimuth and hence $p_\Phi(\phi_{c,l}^{\mathrm{AOA}}) \sim \mathcal{U}[0, 2\pi) \; \forall c, l$. On the other hand, we cannot make such simple assumptions concerning the global AOD and AOA PES since they depend on a number of factors, such as user location and down-tilt angle of the antenna array. We therefore give three different cases for the PES. Namely, two opposing cases: wide and narrow PES, as well as the commonly used Von Mises distributed PES [46], [47], detailed below:

1) *Wide PES*: The PES has a wide, uniform distribution, i.e., $p_\Theta(\theta_{c,l})$ is constant over $[0, \pi) \; \forall c, l$. This is the case for antennas which are isotropic at the TX and an isotropic channel at the RX.

2) *Narrow PES*: The PES has a narrow, uniform distribution, i.e., $p_\Theta(\theta_{c,l})$ is constant over $\theta_0 - \Delta\theta_{c,l}$ and $\theta_0 + \Delta\theta_{c,l} \; \forall c, l$, where $\Delta\theta_{c,l}$ is a small elevation intra-cluster subpath offset with respect to the central cluster angle, θ_0. Here, all clusters have the same elevation central cluster angle, θ_0. However, the subpaths in each cluster are random. The narrow PES SC is best suited to the case of directive antennas and channels of sparse elevation spectra.

3) *Von Mises PES*: The PES is distributed according to the Von Mises distribution [46], [47], i.e., $p_\Theta(\theta_{c,l}) \sim \exp(\kappa\cos(\theta_{c,l} - \mu))/2\pi I_0(\kappa)$, with mean μ and variance $1 - (I_1(\kappa)/I_0(\kappa))$, where κ is the concentration parameter and $I_0(\cdot)$ denotes the zeroth order modified Bessel function.

C. System Aspects

In mmWave channels, 5G BSs are expected to have hundreds of antenna elements (loosely referred to in the industry as massive MIMO). It is currently envisioned that a BS will have at least 256 antenna elements (128 x-pol elements) in a URA topology [2], which is to be constructed by four 64 element panels [1]. While users are likely to have 16 antenna elements in a 4×4 URA configuration [1]. In addition the base station will also support multiple users in the same time slot and frequency resource. The antennas are not just passive antenna elements as exist today. A large part of the RF hardware (such as power amplifiers, phase shifters, summers for BF, duplexer filters, etc) are all situated in backplanes behind the antenna [2]. Furthermore some higher layer processing may also be done at the antenna side to reduce front haul
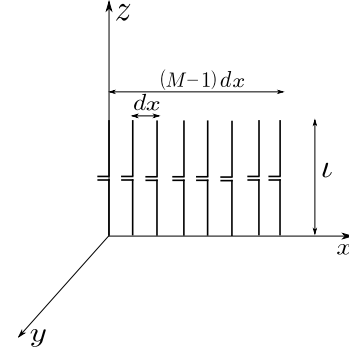

Fig. 1: ULA antenna topology on the x-axis with M dipole antennas, of length ι, with an inter-element spacing of dx.

requirements. Due to the sparse nature of the mmWave channel the number of RF chains much less than the total number of TX antenna elements. This is the motivation to deploy HBF.

Due to space limitations it is not possible to consider the impact of all of these issues and more in this manuscript. Consequently we limit ourselves here to analysing the performance of several antenna topologies (discussed in Section II-E) consisting of dipole antenna elements with 3D SC and MC (discussed in Section II-D), where the S-V channel model is used. The S-V model lends itself to closed form analysis yet it is closely related to the standardised 3GPP model. Furthermore, the HBF rate performance is investigated in a mmWave channel for both dipole and x-pol antenna arrays, using the OMP algorithm [22].

D. Mutual Coupling Model

We consider the MC between (ideal) dipole antenna elements considering that they are terminated by the terminal impedance. While multi-port matching networks could potentially alleviate the impact of MC, these are generally difficult to implement for the large antenna arrays considered in this paper [51], [52]. The global MC matrix is expressed as [17], [28]

$$\mathbf{Z} = (Z_\mathrm{A} + Z_\mathrm{L})(\mathbf{\Xi} + Z_\mathrm{L}\mathbf{I}_M)^{-1}, \qquad (4)$$

where Z_A is the antenna impedance, Z_L is the load or termination impedance and $\mathbf{\Xi}$ is the mutual impedance matrix given by [53]

$$\mathbf{\Xi} = \begin{bmatrix} Z_\mathrm{A} & Z_\mathrm{M}^{1,2} & \cdots & Z_\mathrm{M}^{1,M-1} & Z_\mathrm{M}^{1,M} \\ Z_\mathrm{M}^{2,1} & Z_\mathrm{A} & \cdots & Z_\mathrm{M}^{2,M-1} & Z_\mathrm{M}^{2,M} \\ \vdots & \vdots & \vdots & \vdots & \vdots \\ Z_\mathrm{M}^{M,1} & Z_\mathrm{M}^{M,2} & \cdots & Z_\mathrm{M}^{M,M-1} & Z_\mathrm{A} \end{bmatrix}, \qquad (5)$$

if MC is modelled at the TX. $Z_\mathrm{M}^{m,m'}$ denotes the mutual impedance between antenna elements $m, m' \in 1, \ldots M$. The mutual impedances are obtained by employing the electromotive force method due to its numerical convenience [31], [53].

E. Antenna Array Topologies

We consider the following dipole antenna array topologies:
1) A ULA placed on the x, y-plane
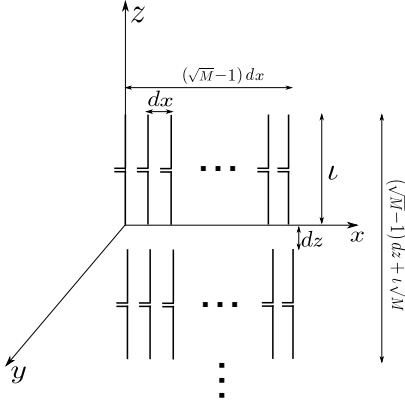2) A URA with one dimension parallel to the z-axis and another dimension placed on the x, y-plane.

Fig. 2: URA antenna topology on the x, z-plane consisting of $\sqrt{M}$ dipoles on the x-axis, with an inter-element spacing of dx, and $\sqrt{M}$ dipoles on the z-axis, with an inter-element spacing of dz. Each dipole antenna element is of length ι.
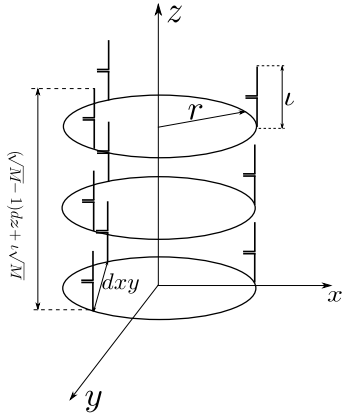

Fig. 3: UCA antenna topology with $\sqrt{M}$ x, y-plane circles of dipole antennas separated on the z-axis by dz. Each x, y-plane circle of antennas has radius r and inter-element spacing dxy. Each dipole antenna element is of length ι.

3) A UCA where a number of x, y-plane circles of antennas are stacked parallel to the z-axis.

The ULA, URA and UCA antenna topologies are shown in Figures 1, 2 and 3, respectively. For both the URA and UCA, we assume that the number of antennas parallel to the x, y-plane are the same as the number of antennas parallel to the z-axis. The antenna array response vectors for each topology are given in (2) and (3), where the TX and RX antenna location matrices, $\mathbf{W}_{\text{TX}}$ and $\mathbf{W}_{\text{RX}}$, respectively, are topology specific.

III. SPATIAL CORRELATION

In this section, we derive closed-form expressions for the SC of the S-V channel given in (1), for wide, narrow and Von Mises PES. The derived expressions can be used to model the SC at either the TX or RX. Without loss of generality, the notation, results and conclusions in this section are obtained for SC antenna elements $m, m' \in 1, \dots, M$ at the TX.

Lemma 1: The SC between two TX antenna elements m, m', with $\mathrm{p}_{\Phi}(\phi_{c,l}^{\text{AOD}}) \sim \mathcal{U}[0, 2\pi)$ $\forall c, l$, and for a general $\mathrm{p}_{\Theta}(\theta_{c,l}^{\text{AOD}})$,
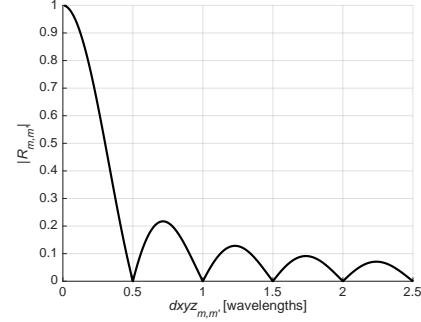

Fig. 4: Wide AOD PES SC magnitude, $|R_{m,m'}|$, between two TX antennas, m and m', as a function of their 3D inter-element spacing, $dxyz_{m,m'}$.

is given as

$$
R_{m,m'} = \sum_{c=1}^{C} \sum_{l=1}^{L} \int_{\theta_{c,l}^{\text{AOD}}} \frac{\exp\left(j2\pi dz_{m,m'} \cos(\theta_{c,l}^{\text{AOD}})\right)}{CL} \times
$$
$$
J_0\left(2\pi dxy_{m,m'} \sin(\theta_{c,l}^{\text{AOD}})\right) \mathrm{p}_{\Theta}(\theta_{c,l}^{\text{AOD}}) \sin(\theta_{c,l}^{\text{AOD}}) d\theta_{c,l}^{\text{AOD}}, \quad (6)
$$

where $J_0(\cdot)$ denotes the zeroth order Bessel function of the first kind, $dx_{m,m'} = dx_m - dx_{m'}$, $dy_{m,m'} = dy_m - dy_{m'}$ and $dz_{m,m'} = dz_m - dz_{m'}$ denote the distance in wavelengths between antenna element m and m' relative to the x, y and z axes, respectively. $dxy_{m,m'} = \sqrt{dx_{m,m'}^2 + dy_{m,m'}^2}$ is the distance in wavelengths between antenna element m and m' on the x, y-plane.

Proof: see Appendix A.

A. Wide AOD PES

Theorem 1: For $\mathrm{p}_{\Theta}\left(\theta_{c,l}^{\text{AOD}}\right)$ constant over $[0, \pi)$ $\forall c, l$, the SC between two TX antenna elements m, m', is

$$
R_{m,m'} = \sum_{c=1}^{C} \sum_{l=1}^{L} \frac{\operatorname{sinc}(2dxyz_{m,m'})}{CL} = \operatorname{sinc}(2dxyz_{m,m'}),
$$
$$(7)$$

where $\operatorname{sinc}(x) = \sin(\pi x)/\pi x$ denotes the normalized sinc function and $dxyz_{m,m'} = \sqrt{dxy_{m,m'}^2 + dz_{m,m'}^2}$ is the distance in wavelengths between antenna elements m and m' in 3D Cartesian coordinates.

Proof: see Appendix B.

From (7), we observe that:

- Increasing the distance between any two TX antennas by the same amount in any direction decorrelates the two antennas equally (non-monotonically).
- The nulls of $|R_{m,m'}|$ (or zero crossings of $R_{m,m'}$) occur when $dxyz_{m,m'} = n/2$ for $n \in \mathbb{Z}^+$, i.e., an antenna array can experience zero SC if adjacent antennas are placed at multiples of a half wavelength. Although this can be achieved easily with a ULA, it cannot be achieved with the URA and UCA topologies, as antenna elements spacings are not always a multiple of a half-wavelength.

In Figure 4 we show the wide AOD PES SC magnitude, $|R_{m,m'}|$, between two TX antennas, m, m', as a function of

their 3D inter-element spacing[4], $dxyz_{m,m'}$. It can be seen that the height of the SC peaks decays as $dxyz_{m,m'}$ increases.

B. Narrow AOD PES

Theorem 2: For $p_\Theta(\theta_{c,l}^{\text{AOD}})$ constant over $[\theta_0^{\text{AOD}} - \Delta\theta_{c,l}^{\text{AOD}}, \theta_0^{\text{AOD}} + \Delta\theta_{c,l}^{\text{AOD}}]\ \forall c,l$, where $\Delta\theta_{c,l}^{\text{AOD}}$ is small, the SC between TX antenna elements m, m', can be approximated as

$$R_{m,m'} \approx \exp\left(j2\pi dz_{m,m'}\cos(\theta_0^{\text{AOD}})\right)$$
$$\times J_0\left(2\pi dxy_{m,m'}\sin(\theta_0^{\text{AOD}})\right). \quad (8)$$

Proof: see Appendix C.

Here we draw some insights into the narrow AOD PES TX SC, given in (8):

- The expression in (8) is independent of the intra-cluster elevation AOD offsets, $\Delta\theta_{c,l}^{\text{AOD}}$, and therefore the intra-cluster elevation AOD spreads, because the multiple rays of each cluster are approximated by the constant elevation central cluster AOD, θ_0^{AOD}. For the same reason, $R_{m,m'}$ is independent of the number of subpaths, L.
- $R_{m,m'}$ is independent of azimuth angles because the AOD PAS is uniform over its entire range.
- $R_{m,m'}$ decreases non-monotonically with $dxy_{m,m'}$, as increased x,y-plane spacing tends to reduce $|R_{m,m'}|$ since it affects the modulus of (8) via the Bessel function.
- For a fixed $dxy_{m,m'}$, the modulus, $J_0\left(2\pi dxy_{m,m'}\sin(\theta_0^{\text{AOD}})\right)$, is reduced when $\sin(\theta_0^{\text{AOD}})$ is maximized. This occurs when $\theta_0^{\text{AOD}} = \pi/2$, i.e., when the central AOD is broadside to the TX antenna array with respect to the z-axis. At this elevation AOD, the phase shift disappears and the resultant SC becomes $R_{m,m'} = J_0\left(2\pi dxy_{m,m'}\right)$, i.e., only a function of the x,y-plane inter-element spacings.
- When the central AOD is end-fire to the TX antenna array with respect to the z-axis, the resultant SC becomes $R_{m,m'} = \exp\left(j2\pi dz_{m,m'}\right)$, i.e., only a function of the z-axis inter-element spacings. Note that here the SC has a magnitude of 1. This is a mathematical peculiarity and is due to the fact that in this scenario there is just a phase shift in the elevation domain between m and m'.
- This scenario can be generalized to a narrow angular spread within clusters of fixed but different central cluster AODs. Here, the global PES is not narrow, but the PES of subpaths within a cluster is narrow. Here, (8) becomes

$$R_{m,m'} = \frac{1}{C}\sum_{c=1}^{C}\exp\left(j2\pi dz_{m,m'}\cos(\theta_{0,c}^{\text{AOD}})\right)$$
$$\times J_0\left(2\pi dxy_{m,m'}\sin(\theta_{0,c}^{\text{AOD}})\right). \quad (9)$$

In this scenario, the phase shift, $\exp\left(j2\pi dz_{m,m'}\cos(\theta_0^{\text{AOD}})\right)$, is able to decrease $|R_{m,m'}|$ non-monotonically. A larger z-axis spacing increases the phase oscillations and hence the C components are more likely to be out of phase and cancel, reducing $|R_{m,m'}|$ by a different mechanism than $dxy_{m,m'}$.

To date, all 3D channel model measurement campaigns express the elevation AOD central cluster angles as some small

---

[4]Note that all results presented in this section are without MC. In Section V, the effects of MC is considered.

---

random variation around the LOS angle to the user, ϑ^{AOD} [9], [14], [39]. Any downtilting of the TX antenna array would affect the relative LOS angle, ϑ^{AOD}, however, we assume no mechanical downtilting of any antenna arrays. To examine the accuracy of (8) to the true SC for increasing intra-cluster subpath offsets, $\Delta\theta_{c,l}^{\text{AOD}}$, we assume $\theta_0^{\text{AOD}} = \vartheta^{\text{AOD}}$ following [8]. Therefore,

$$R_{m,m'} = \exp\left(j2\pi dz_{m,m'}\cos(\vartheta^{\text{AOD}})\right)$$
$$\times J_0\left(2\pi dxy_{m,m'}\sin(\vartheta^{\text{AOD}})\right). \quad (10)$$

In Figure 5 we show good agreement between the magnitude of the mean SC between two TX antennas, $m, m' \in 1, \ldots, M$, for narrow AOD PES as a function of their x, y-plane inter-element spacing, $dxy_{m,m'}$, and elevation AOD subpath offsets, $\Delta\theta_{c,l}^{\text{AOD}}$. The SC is averaged over 10^4 LOS angles, ϑ^{AOD}, where the user is located between 30 and 200m based on area coverage with a TX height of 17m and a RX height of 2m [8]. It can be seen that as the elevation AOD subpath offsets, $\Delta\theta_{c,l}^{\text{AOD}}$, are increased, the narrow AOD PES becomes a less accurate approximation to the SC. This is intuitive since we are approximating the SC in (6) by a single elevation AOD. However, the simple narrow AOD PES results are surprisingly accurate even up to $\Delta\theta_{c,l}^{\text{AOD}} = 30°\ \forall c,l$. We also see that the peaks of the SC are slightly reduced in magnitude as the elevation AOD subpath offsets, $\Delta\theta_{c,l}^{\text{AOD}}$, are increased. This is a result of greater angular diversity in the system and the extreme case is the wide AOD PES, shown in Figure 4. Furthermore, we observe that the nulls of the SC magnitude occur for smaller distances as $\Delta\theta_{c,l}^{\text{AOD}}$ is reduced. This is because the LOS elevation angle to the user, ϑ^{AOD}, is nearly always relatively close to $90°$ (due to user location) as $\Delta\theta_{c,l}^{\text{AOD}}$ becomes smaller, therefore increasing the Bessel function argument, i.e., $\sin(\theta_{c,l}^{\text{AOD}}) = \sin(\theta_0^{\text{AOD}} + \Delta\theta_{c,l}^{\text{AOD}}) = \sin(\vartheta^{\text{AOD}} + \Delta\theta_{c,l}^{\text{AOD}}) \approx \sin(\vartheta^{\text{AOD}}) \approx 1\ \forall c,l$, for small $\Delta\theta_{c,l}^{\text{AOD}}$. On the other hand, as $\Delta\theta_{c,l}^{\text{AOD}}$ increases, there becomes a higher likelihood that the magnitude of $\sin(\theta_{c,l}^{\text{AOD}})$ is reduced for a particular ray. The extreme case, where the first null occurs at a distance of $dxy_{m,m'} = 0.5$, is equivalent to the wide AOD PES shown in Figure 4.

C. Von Mises AOD PES

Theorem 3:

For $p_\Theta(\theta_{c,l}^{\text{AOD}}) \sim \exp\left(\kappa\cos(\theta_{c,l}^{\text{AOD}} - \mu)\right)/2\pi I_0(\kappa)$, the SC between TX antenna elements m, m', can be approximated by

$$R_{m,m'} \approx \frac{\text{sinc}\left(2\sqrt{dxy_{m,m'}^2 + \left(dz_{m,m'} - j\frac{\kappa\cos(\mu)}{2\pi}\right)^2}\right)}{\text{sinc}\left(j\frac{\kappa\cos(\mu)}{\pi}\right)}. \quad (11)$$

Proof: see Appendix D.

From (11) it can be seen that:

- Increasing the inter-element spacing on the either the x, y-plane or z-axis decreases the SC non-monotonically.
- If $dxy_{m,m'} = 0$, $R_{m,m'} = \text{sinc}\left(2dz_{m,m'} - j\frac{\kappa\cos(\mu)}{\pi}\right)/\text{sinc}\left(j\frac{\kappa\cos(\mu)}{\pi}\right)$. Apart from when $dz_{m,m'} = 0$,
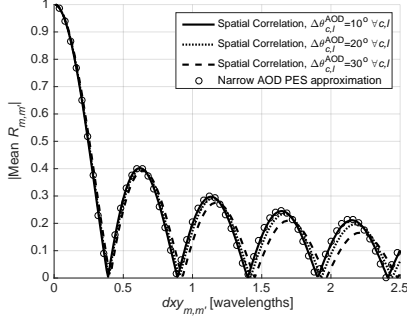
Fig. 5: Magnitude of the mean SC between two TX antennas, m and m', for narrow AOD PES as a function of their x, y-plane inter-element spacing, $dxy_{m,m'}$, and elevation AOD subpath offsets, $\Delta\theta_{c,l}^{\text{AOD}}$. $dz_{m,m'} = 0$

$R_{m,m'}$ can never be zero since $2dz_{m,m'} \neq j\kappa\cos(\mu)/\pi \ \forall dz_{m,m'}$.

- If $dz_{m,m'} = 0$, the SC becomes $R_{m,m'} =$
  $\text{sinc}\left(2\sqrt{dxy_{m,m'}^2 - \left(\frac{\kappa\cos(\mu)}{2\pi}\right)^2}\right) \Big/ \text{sinc}\left(j\frac{\kappa\cos(\mu)}{\pi}\right)$
  and the nulls of $|R_{m,m'}|$ occur when $dxy_{m,m'} = \sqrt{\frac{n}{4} + \left(\frac{\kappa\cos(\mu)}{2\pi}\right)^2}$ for $n \in \mathbb{Z}^+$. For example, at $\mu = \pi/2$ and $\mu = \pi/3$, the first null of $|R_{m,m'}|$ occurs at $dxy_{m,m'} = 1/2$ and $dxy_{m,m'} = \sqrt{\frac{1}{4} + \left(\frac{\kappa}{2\pi}\right)^2}$ wavelengths, respectively.
- For $\mu = \pi/2$, $R_{m,m'}$ becomes equal to the wide AOD PES SC in (7).
- As μ approaches 0 or π, $R_{m,m'}$ increases.
- As the concentration parameter $\kappa \to 0$, the distribution of $\theta_{c,l}^{\text{AOD}}$ becomes uniform over $[0, \pi) \ \forall c, l$ and $R_{m,m'}$ becomes equal to the wide AOD PES SC in (7).
- As the concentration parameter $\kappa \to \infty$, the AOD PES becomes infinitesimally small and thus $R_{m,m'} \approx 1$.

In Figure 6 we show the accuracy of the mean SC between two TX antennas, m, m', for a Von Mises AOD PES approximation as a function of their x, y-plane inter-element spacing, $dxy_{m,m'}$. It can be seen that the approximation is exact for $\kappa = 0$, $\mu = \pi/2$, $\mu = 0$ and $\mu = \pi$. For $\kappa = 2$ and $\mu = 2\pi/3$, the approximation is reasonably good for small spacings and large spacings.

IV. CONVERGENCE TO MASSIVE MIMO: DIAGONAL DOMINANCE

In this section, we explore the rate of convergence of a user's channel to favourable massive MIMO propagation [5], [48] for the different antenna topologies, as the number of RX antennas, Q, becomes large. It is assumed that there is no power variation over the array aperture. We measure the convergence of a user's channel by defining the *diagonal dominance*, δ, as

$$\delta = \frac{\frac{1}{Q(Q-1)}\sum_{q=1}^{Q}\sum_{q'=1,q'\neq q}^{Q}\left|\mathbb{E}\left[\mathbf{h}_q\mathbf{h}_{q'}^{\text{H}}\right]\right|}{\frac{1}{Q}\sum_{q=1}^{Q}\mathbb{E}\left[\mathbf{h}_q\mathbf{h}_q^{\text{H}}\right]}, \quad (12)$$
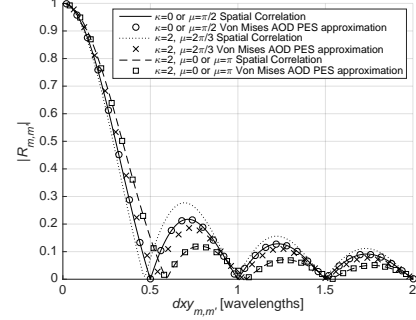

Fig. 6: SC magnitude between TX antennas, m and m' vs $dxy_{m,m'}$, for a Von Mises AOD PES.

where $\mathbf{h}_q$ denotes the qth row of $\mathbf{H}$. Note that δ will converge to zero when channels between antenna elements, of the user, become orthogonal, i.e., the diagonal elements become large relative to the off-diagonals in the summations. Note here that the diagonal dominance is a function of the user antenna array and therefore (12) is dependent on the number of user antennas, Q, and AOAs, rather the number of BS antennas, M, and AODs[5].

Lemma 2: Given the S-V channel model in (1) and an AOA PAS of $p_\Phi(\phi_{c,l}^{\text{AOA}}) \sim \mathcal{U}[0, 2\pi) \ \forall c, l$, as discussed in Section II-B, the diagonal dominance can be written as

$$\delta = \frac{1}{Q(Q-1)}\sum_{q=1}^{Q}\sum_{q'=1,q'\neq q}^{Q}\frac{1}{CL}\left|\sum_{c=1}^{C}\sum_{l=1}^{L}\mathbb{E}\left[\exp\left(j2\pi \times \right.\right.\right.$$
$$\left.\left.\left. dz_{q,q'}\cos(\theta_{c,l}^{\text{AOA}})\right)J_0\left(2\pi dxy_{q,q'}\sin(\theta_{c,l}^{\text{AOA}})\right)\right]\right|. \quad (13)$$

Proof: see Appendix E.

We now give the three cases of AOA PES: wide, narrow and Von Mises, in Sections IV-A, IV-B and IV-C respectively.

A. Wide AOA PES

Evaluating the expectation in (13) for a wide AOA PES, i.e., $p_\Theta(\theta_{c,l}^{\text{AOA}})$ constant over $[0, \pi) \ \forall c, l$, δ gives

$$\delta = \frac{1}{Q(Q-1)}\sum_{q=1}^{Q}\sum_{q'=1,q'\neq q}^{Q}\left|\text{sinc}\left(2dxyz_{q,q'}\right)\right|, \quad (14)$$

where the steps are analogous to the wide AOD PES SC, given in Appendix B, and $dxyz_{q,q'}$ denotes the distance in wavelengths between antenna elements q and q' in 3D Cartesian coordinates. From (14), we observe that:

- Increasing the distance between two antennas by the same amount in any direction decreases δ equally (non-monotonically).
- Assuming uniform spacings in any direction, δ will be zero when $dxyz_{q,q'} = n/2$ for $n \in \mathbb{Z}^+$. This can be achieved easily with a ULA, however it cannot be achieved with the URA and UCA topologies, as antenna elements spacings are not always a multiple of a $1/2$ wavelength.

---

[5]Since we are considering a DL channel, the diagonal dominance is defined for a particular user. However, all the analysis holds in the case of an UL channel, where the diagonal dominance would be defined for a BS.
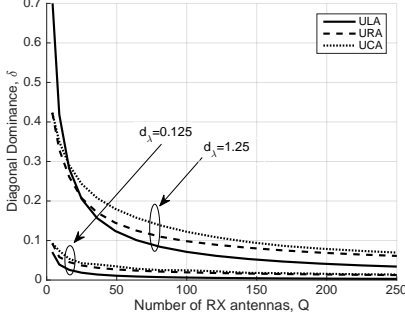
Fig. 7: Diagonal dominance of a user's channel, δ, for a wide AOA PES, as a function of Q and d_λ.

Fig. 8: Diagonal dominance of a user's channel, δ, for a narrow AOA PES, as a function of Q and d_λ.

In Figure 7, we show the diagonal dominance of a user's channel, δ, for a wide AOA PES, as a function of the number of receive antenna elements, Q, antenna topology and antenna inter-element spacing. d_λ denotes the antenna inter-element spacing in wavelengths. It can be seen that an increase in inter-element spacing from $d_\lambda = 0.125$ to 1.25 wavelengths results in nearly an order of magnitude decrease in δ. The ULA has lower values of δ as it has fewer adjacent antenna elements, compared with the URA and UCA. Also, as Q increases, the value of δ for the URA and UCA converge to be similar.

B. Narrow AOA PES

Analogous to the steps in Appendix C, the diagonal dominance of a user's channel, with a narrow AOA PES, can be approximated as

$$\delta = \frac{1}{Q(Q-1)} \sum_{q=1}^{Q} \sum_{q'=1, q' \neq q}^{Q} \left| \exp\left(j2\pi dz_{q,q'} \cos(\theta_0^{\text{AOA}})\right) \right.$$
$$\left. \times J_0\left(2\pi dxy_{q,q'} \sin(\theta_0^{\text{AOA}})\right) \right| \quad (15)$$

$$= \sum_{q=1}^{Q} \sum_{q'=1, q' \neq q}^{Q} \frac{\left| J_0\left(2\pi dxy_{q,q'} \sin(\theta_0^{\text{AOA}})\right) \right|}{Q(Q-1)}, \quad (16)$$

since $|\exp(jx)| = 1$. From (16), we can draw some insights:

- δ is independent of $dz_{q,q'}$.
- As discussed for the narrow AOD PES SC in Section III-B, δ is independent of the angular spreads, the number of subpaths, L, and azimuth angles. δ decreases non-monotonically with $dxy_{q,q'}$.
- For a fixed θ_0^{AOA}, differences in δ between the URA and UCA come from the oscillatory nature of $J_0(2\pi dxy_{q,q'})$, which is a function of the x,y-plane inter-element spacings. Note that $dxy_{q,q'}^{\text{URA}} \geq dxy_{q,q'}^{\text{UCA}}$ with equality only if $q = q' \pm 1$, where the layout of the antenna topologies are described in Section II-E.
- If $\theta_0^{\text{AOA}} = \vartheta^{\text{AOA}}$ as in [8], then

$$\delta = \sum_{q=1}^{Q} \sum_{q'=1, q' \neq q}^{Q} \frac{\left| J_0\left(2\pi dxy_{q,q'} \sin(\vartheta^{\text{AOA}})\right) \right|}{Q(Q-1)}. \quad (17)$$

In Figure 8, we show the diagonal dominance of a user's channel, δ, for a narrow AOA PES, where $\theta_0^{\text{AOA}} = \vartheta^{\text{AOA}}$, as in
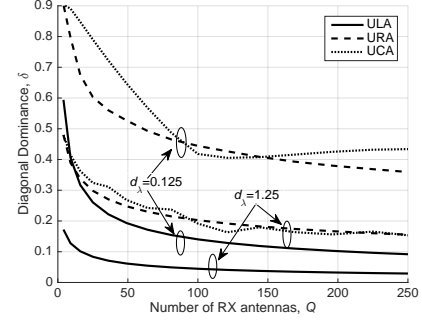
(17) [8]. As was the case in the wide AOA PES scenario, an increase in inter-element spacing from $d_\lambda = 0.125$ to 1.25 wavelengths results in a large decrease in δ. Since δ is independent of the z-axis inter-element spacing, the ULA now performs significantly better than the URA and UCA topologies. The slope of the UCA δ is not smooth, as seen for the ULA and URA topologies, and intersects the URA δ at different numbers of RX antenna elements, Q. For large antenna spacings, the diagonal dominance of the URA and UCA converge to similar spacings. Comparing Figures 7 and 8, δ in the narrow AOA PES case is larger than the wide AOA PES since, in general, the magnitude of $|J_0(2\pi x)|$ is much larger than $|\text{sinc}(2x)|$.

C. Von Mises AOA PES

If $\text{p}_\Theta(\theta_{c,l}^{\text{AOA}}) \sim \exp\left(\kappa \cos(\theta_{c,l}^{\text{AOA}} - \mu)\right)/2\pi I_0(\kappa)$, δ can be approximated by

$$\delta \approx \frac{1}{Q(Q-1)} \left| \text{sinc}\left(j\frac{\kappa \cos(\mu)}{\pi}\right) \right|^{-1} \sum_{q=1}^{Q} \sum_{q'=1, q' \neq q}^{Q}$$
$$\left| \text{sinc}\left(2\sqrt{dxy_{q,q'}^2 + \left(dz_{q,q'} - j\frac{\kappa \cos(\mu)}{2\pi}\right)^2}\right) \right|, \quad (18)$$

where the steps are analogous to the Von Mises AOD PES SC, given in Appendix D. From (18):

- Increasing the inter-element spacing on the either the x,y-plane or z-axis decreases δ non-monotonically.
- If $dxy_{q,q'} = 0$, δ is never zero apart from when $dz_{q,q'} = 0$, since $2dz_{q,q'} \neq j\kappa \cos(\mu)/\pi \ \forall dz_{q,q'}$.
- If $dz_{q,q'} = 0$, δ is zero when $dxy_{q,q'} = \sqrt{\frac{n}{4} + \left(\frac{\kappa \cos(\mu)}{2\pi}\right)^2}$ for $n \in \mathbb{Z}^+$.
- For $\mu = \pi/2$, δ becomes equal to the wide AOA PES diagonal dominance in (14).
- As μ approaches 0 or π, δ increases.
- As the concentration parameter $\kappa \to 0$, the distribution of $\theta_{c,l}^{\text{AOA}}$ becomes uniform over $[0, \pi) \ \forall c, l$ and δ becomes equal to the wide AOA PES δ in (14).
- As the concentration parameter $\kappa \to \infty$, the AOA PES becomes infinitesimally small and thus $\delta \to \infty$.

For reasons of space, we do not numerically simulate the Von Mises AOA PES diagonal dominance.

V. Numerical Results

In this section the effects of different antenna array topologies on the resultant SC, eigenvalue structure and user rate of a mmWave system are analysed, with and without MC. The HBF performance is also shown in a mmWave system for both dipole and x-pol antenna elements, where the orthogonal matching pursuit (OMP) algorithm [22] is used. In Sections V-A and V-B, the effects of MC, on SC and eigenvalue structure, respectively, are investigated for the two opposing SC cases: wide and narrow AOD PES. Here, the expressions derived in Section III are used, given in (7) and (10) for the two respective cases, i.e., there is no channel randomness in these results. In Sections V-C and V-D, the rate of a 28 GHz mmWave channel [8] is simulated without beamforming, and with HBF, respectively.

In all cases where MC is modelled, we use an antenna impedance of $Z_A = 73 + j42.5$ Ω [53], [54]. Ideally the load impedance would then be the conjugate antenna impedance, however this is difficult to do in practice. We are therefore interested in the effects of imperfect impedance matching on a number of system metrics. Thus, we show the effects of the ideal load impedance, the conjugate antenna impedance $Z_L = Z_A^* = 73 - j42.5$ Ω, and a completely different value of $Z_L = 50$ Ω, as used in [28]. The mutually coupled channel matrix of an arbitrary user, $\overline{\mathbf{H}}$, is given by [55]

$$\overline{\mathbf{H}} = \mathbf{Z}_{RX}\mathbf{H}\mathbf{Z}_{TX}, \tag{19}$$

where $\mathbf{Z}_{RX}$ and $\mathbf{Z}_{TX}$ denote the $Q \times Q$ RX and $M \times M$ TX MC matrices, respectively, as given in (4).

A. Impact of Antenna Separation

All results in this section are applicable to either the TX or RX antenna array. Without loss of generality we explore the effects of SC and MC with multiple antennas employed at the TX, i.e., $\mathbf{Z}_{RX} = \mathbf{I}_Q$ in (19).

To draw insight into how different array topologies are affected by MC, we numerically show its effects on three different dipole antenna pairs [53]:

- *Side-by-side*: where $dxy_{m,m'} \neq 0$ and $dz_{m,m'} = 0$ for $m, m' \in 1, \dots, M$.
- *Collinear*: where $dxy_{m,m'} = 0$ and $dz_{m,m'} \neq 0$ for $m, m' \in 1, \dots, M$.
- *Parallel-in-echelon*: where $dxy_{m,m'} \neq 0$ and $dz_{m,m'} \neq 0$ for $m, m' \in 1, \dots, M$. For simplicity, we consider the case where $dxy_{m,m'} = dz_{m,m'}$.

1) Wide AOD PES: In Figure 9 we show the *normalized* magnitude of a wide AOD PES SC, $|R_{m,m'}|/|R_{m,m}|$, with and without MC between two TX antennas, $m, m' \in 1, \dots, M$, as a function of their inter-element spacing, $d_{m,m'}$, for the three different antenna configurations listed above. When only SC is modelled, $R_{m,m'}$ is given as derived in Section III. When MC is added, $R_{m,m'} = \mathbb{E}[\overline{\mathbf{h}}_m^H \overline{\mathbf{h}}_{m'}] = Z_{TX,m,m}^H \mathbb{E}[\mathbf{h}_m^H \mathbf{h}_{m'}] Z_{TX,m',m'}$, since the elements of the MC matrix are a function of deterministic parameters [53], where $\overline{\mathbf{H}}$ is defined in (19) and $\mathbf{h}_m$ is the mth column of $\mathbf{H}$. For the side-by-side antenna configuration, the effects of MC are more obvious at smaller antenna separations. For

example, it can be seen that MC reduces the magnitude of the normalized SC for inter-element spacings $d_{m,m'} < 0.37$ wavelengths and $d_{m,m'} < 0.43$ wavelengths for $Z_L = 50$ Ω and $Z_L = 73 - j42.5$ Ω, respectively. There is a negligible impact on the SC when antennas are in the collinear configuration, because the ideal dipole radiation pattern has a singularity at its ends and therefore the impinging radiation on (collinear) adjacent antennas is minimal. On the other hand, when antennas are in the parallel-in-echelon configuration, the MC causes a strong increase in the normalized SC and its magnitude is yet to converge to the scenario with no MC, as the other configurations do, even for inter-element spacings of up to $d_{m,m'} = 2.5$ wavelengths. Comparing Figure 9a with Figure 9b, we note that the shape of the decay, before a half-wavelength spacing for the side-by-side configuration, is dependent on the load impedance, Z_L, chosen [29], [31], [54], [56]. The magnitude of the normalized SC peaks for the side-by-side and parallel-in-echelon configurations are reduced when $Z_L = Z_A^*$.

2) Narrow AOD PES: In Figure 10 we show the average normalized magnitude of a narrow AOD PES SC, $|R_{m,m'}|/|R_{m,m}|$, with and without MC as a function of their inter-element spacing, $d_{m,m'}$, for three different antenna configurations. Note that here the normalized SC magnitude, $|R_{m,m'}|/|R_{m,m}|$, is averaged over user locations (to compute ϑ^{AOD} in (10)), where a circular coverage region of radius of 200 m is used [8]. It can be seen that for both values of Z_L in the side-by-side antenna configuration, MC reduces the magnitude of the normalized SC for all inter-element spacings less than $d_{m,m'} = 0.4$ wavelengths. However, two large peaks can be seen at around $d_{m,m'} = 0.65$ and 1.65 wavelengths, where the conjugate impedance matching scenario ($Z_L = Z_A^*$) reduces the magnitude of the peaks and increases the number of nulls. SC for the collinear antennas configuration show no difference when MC is modelled. Both show a magnitude of unity since the AOD between two antennas only has a phase variation. Compared to the wide AOD PES SC (Figure 9), the normalized SC magnitude shows an increase when the AOD PES is narrow (Figure 10) for all cases of antenna configurations with and without MC, over nearly all spacings. This is intuitive and results from a lack of spatial diversity when the AOD PES is narrow. In general, MC can increase or decrease the SC at a given inter-element spacing, dramatically for side-by-side antenna elements, which is consistent with [28], [29], [54], [56].

B. Eigenvalue Structure

In this section, we look at the eigenvalue magnitude vs. the eigenvalue index for spatially correlated TX antenna arrays with and without MC. When only SC is modelled, the eigenvalues of $\mathbb{E}[\mathbf{H}^H\mathbf{H}]$ are considered, while when MC is included, the eigenvalues of $\mathbb{E}[\overline{\mathbf{H}}^H\overline{\mathbf{H}}]$ are considered. Due to space constraints we only show the effect of different load impedances in the (more interesting) scenario of small inter-element antenna spacing. The number of significant eigenvalues provides a measure of the number of streams which can be used for efficient spatial multiplexing [45], [57], [58]. We truncate each figure below -20 dB eigenvalue magnitude, as
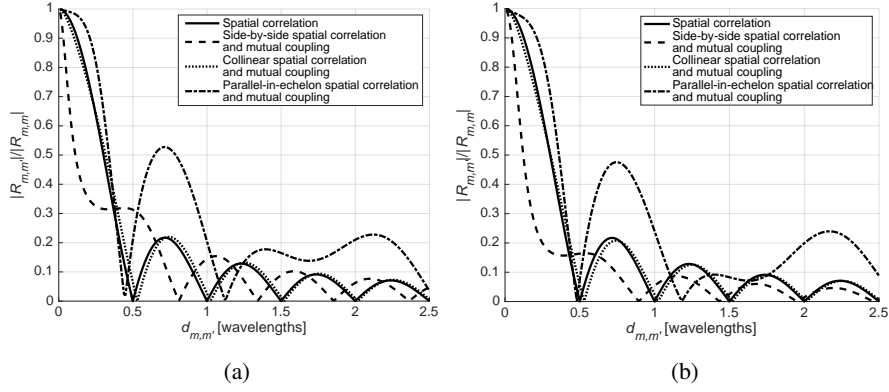
Fig. 9: Normalized magnitude of a wide AOD PES SC, $|R_{m,m'}|/|R_{m,m}|$, with and without MC as a function of $d_{m,m'}$. (a) $Z_L = 50 \ \Omega$. (b) $Z_L = Z_A^* = 73 - j42.5 \ \Omega$. Note that there are a total of 4 curves in each subfigure.
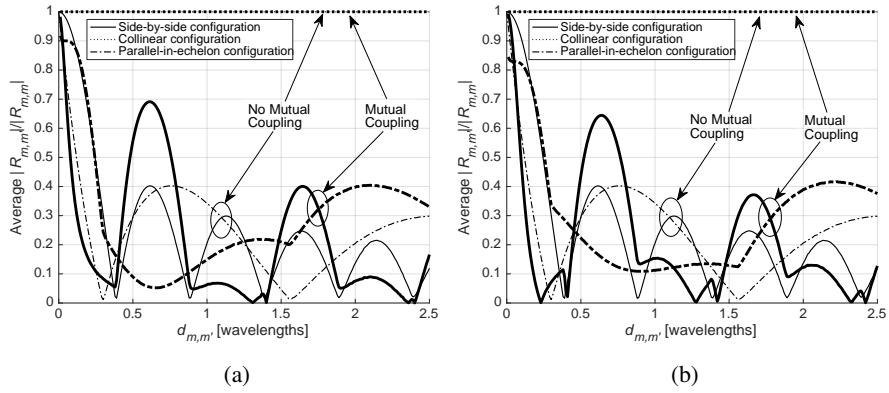

Fig. 10: Average normalized magnitude of a narrow AOD PES SC, $|R_{m,m'}|/|R_{m,m}|$, with and without MC as a function of $d_{m,m'}$. (a) $Z_L = 50 \ \Omega$. (b) $Z_L = Z_A^* = 73 - j42.5 \ \Omega$. Note that there are a total of 6 curves in each subfigure.

these eigenvalues are essentially in the noise floor and do not contribute to the antenna array's spatial multiplexing abilities. We show the eigenvalue magnitude without MC as well as for both cases of unnormalized (main figure) and normalized MC[6] (subfigure), with the aim of determining its impact on the power of the eigenvalues.

1) Wide AOD PES: In Figure 11 we show the eigenvalue magnitude vs eigenvalue index for wide AOD PES spatially correlated TX antenna topologies with and without MC, with $M = 100$ TX antenna elements, for inter-element spacings of $d_\lambda = 0.125$ and $d_\lambda = 1.25$ wavelengths. For small inter-element spacings, MC reduces the magnitude of the largest eigenvalues in all antenna topologies when MC is unnormalized, and only the ULA eigenvalues when MC is normalized. This indicates that the resultant SC, with MC, is having almost no effect on the eigenvalues of the URA and UCA for small inter-element spacings. However, MC is causing a reduction in the magnitude of the largest eigenvalues - which is most evident in the case where $Z_L = Z_A^*$. Here, the UCA has the largest number of eigenvalues above a magnitude of -20 dB, and therefore best spatial multiplexing capabilities.

On the other hand, the ULA has only a small number of eigenvalues which are not very small in magnitude.

For large inter-element spacings, the eigenvalues for all topologies with only SC become more similar, as they are approaching an i.i.d. scenario. When MC is added for large inter-element spacings, the magnitude of the first eigenvalue is increased significantly for the URA and UCA, while the magnitude of the smaller eigenvalues is reduced for these topologies. This is because, even at larger inter-element spacings, there is still a significant increase in SC, when MC is included, for antennas in the parallel-in-echelon configuration, specific to the URA and UCA. Also, at $d_\lambda = 1.25$, there is little difference in eigenvalue structure between normalized and unnormalized MC.

2) Narrow AOD PES: In Figure 12 we show the eigenvalue magnitude vs eigenvalue index for narrow AOD PES spatially correlated antenna topologies with and without MC, for $M = 100$ TX antenna elements, with inter-element spacings of $d_\lambda = 0.125$ and $d_\lambda = 1.25$ wavelengths. The ULA is seen to have a large difference in spatial multiplexing performance when MC is modelled for small inter-element spacings. This is because MC exhibits large variation over different inter-element spacings in the side-by-side normalized SC, as shown in Figure 10. Increasing the inter-element antenna spacings

[6]Normalized MC corresponds to the eigenvalues of $\mathbb{E}[\overline{\mathbf{H}}^H \overline{\mathbf{H}}]$ where $\mathbf{Z}_{TX}$ is normalized to have diagonal entries of 1.
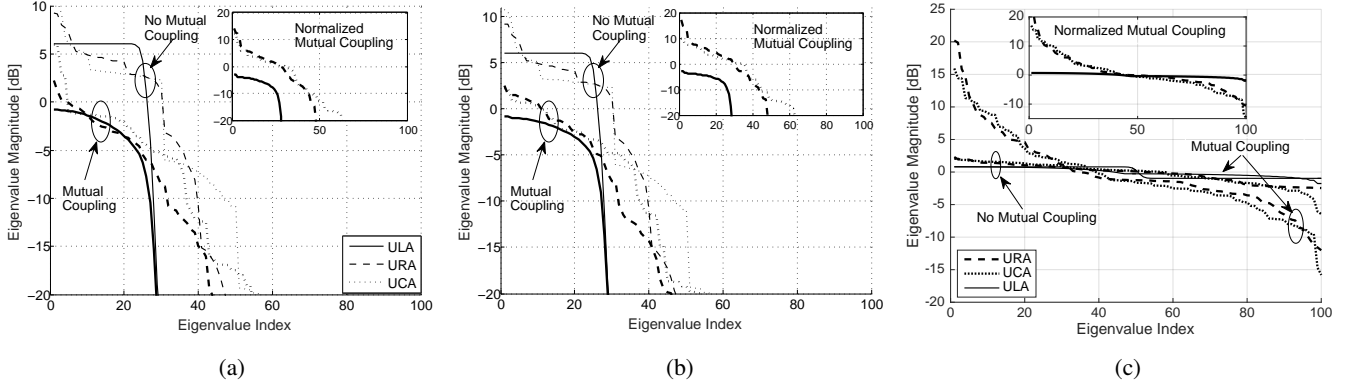
Fig. 11: Eigenvalue magnitude vs eigenvalue index for wide AOD PES SC with and without MC, for $M = 100$. (a) $d_\lambda = 0.125$, $Z_L = 50 \ \Omega$. (b) $d_\lambda = 0.125$, $Z_L = Z_A^* = 73 - j42.5 \ \Omega$. (c) $d_\lambda = 1.25$, $Z_L = 50 \ \Omega$.
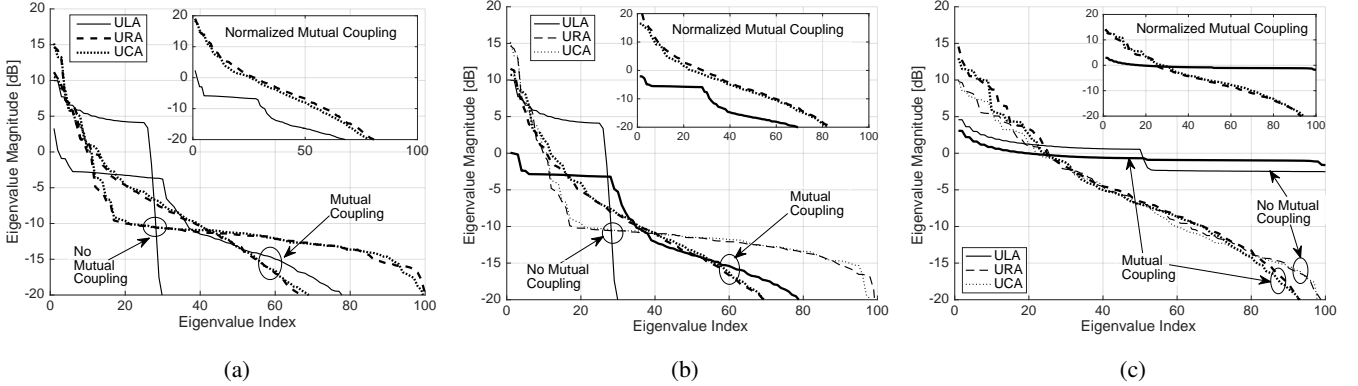

Fig. 12: Eigenvalue magnitude vs eigenvalue index for narrow AOD PES SC with and without MC, for $M = 100$. (a) $d_\lambda = 0.125$, $Z_L = 50 \ \Omega$. (b) $d_\lambda = 0.125$, $Z_L = Z_A^* = 73 - j42.5 \ \Omega$. (c) $d_\lambda = 1.25$, $Z_L = 50 \ \Omega$.

from $d_\lambda = 0.125$ to 1.25 wavelengths improves the performance of all antenna topologies, particularly for the ULA with MC, which has nearly equal eigenvalues. MC causes a power reduction to the largest eigenvalues of the URA and UCA for small spacings, whereas there is a very little power difference for large inter-element spacings.

In general, when MC is modelled the ULA is most affected out of the three antenna topologies, which was also seen for the normalized SC of side-by-side antenna elements. The power scaling effects of MC are more noticeable at small inter-element spacings, where the eigenvalue magnitude of the URA and UCA topologies is diminished (reduced).

C. User Rate without Beamforming

In this section, we explore the impact of MC on user rate as a function of antenna inter-element spacing, the number of antennas and antenna array topology. In all results following, we simulate a 28 GHz mmWave channel [8] and include MC both at the TX and RX. The rate of a user is given by [59]

$$\text{User Rate} = B \log_2 \left| \mathbf{I}_Q + (\rho/M)\overline{\mathbf{H}}\overline{\mathbf{H}}^H \right|, \quad (20)$$

where B is the bandwidth, ρ is the received SNR and the mutually coupled channel matrix, $\overline{\mathbf{H}}$, is given in (19). In order not to mask the effects of SC and MC on the user rate by

large variations in PL, we assume the received SNR, ρ, is constant. We assume perfect channel state information (CSI) is available at the RX for all user rate simulations, where we summarize key simulation parameters[7] in Table I. Since [8] reports no measurable elevation AOD intra-cluster angular spread, we assume the ratio of mean azimuth to elevation intra-cluster angular spreads is the same for AODs as AOAs, i.e., $6.0(10.2/15.5)^\circ = 3.9^\circ$.

1) Impact of Inter-Element Spacing: In Figures 13a and 13b we show the user rate vs inter-element antenna spacing, both with and without MC and $M = Q = 36$, for $Z_L = 50 \ \Omega$ and $Z_L = 73 - j42.5 \ \Omega$, respectively. Due to the very small number of clusters ($C = 1$ or 2 73% of the time [8]), all simulated channels have a poorer performance compared to the, ideal, i.i.d. channel rates [5]. When only SC is modelled, the rates of all antenna topologies increases as the inter-element antenna spacing is increased. The ULA performs the best here as it has fewer adjacent and surrounding antenna

---

[7]It should be noted that many channel model studies at both microwave and mmWave frequencies distribute central cluster azimuth angles from a non-uniform distribution with variance less than 75°, e.g., normal distribution [9], [12], [14], [39], [40]. In other words, all the subpaths are coming from the same general direction. However, this paper assumes the channel model and measurement parameters from [8] and therefore the central cluster azimuth angles are distributed as $\mathcal{U}[0, 2\pi)$.
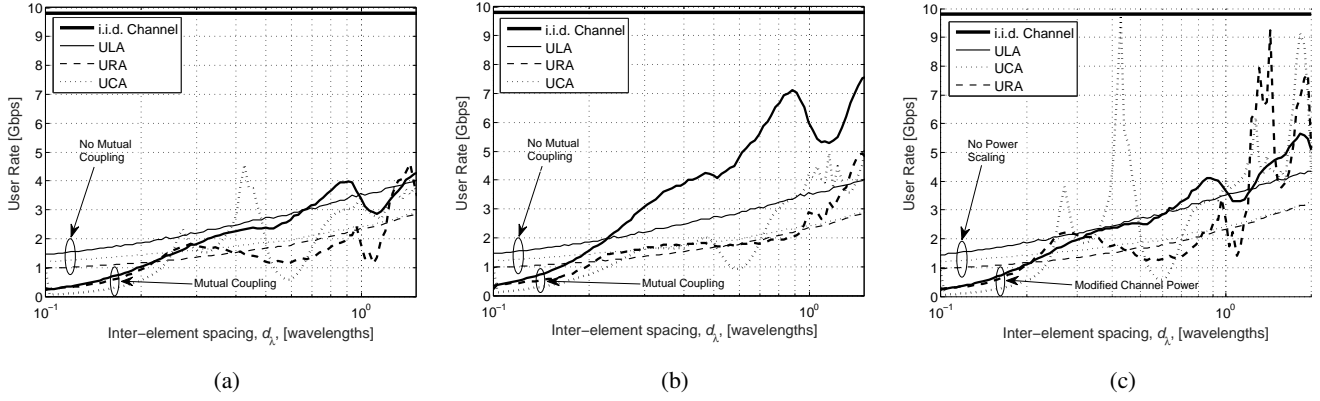
Fig. 13: User rate vs inter-element antenna spacing, d_λ for $M = 36$ TX antennas and $Q = 36$ RX antennas. (a) MC with $Z_L = 50\ \Omega$. (b) MC with $Z_L = 73 - j42.5\ \Omega$. (c) Modified channel power of (a).
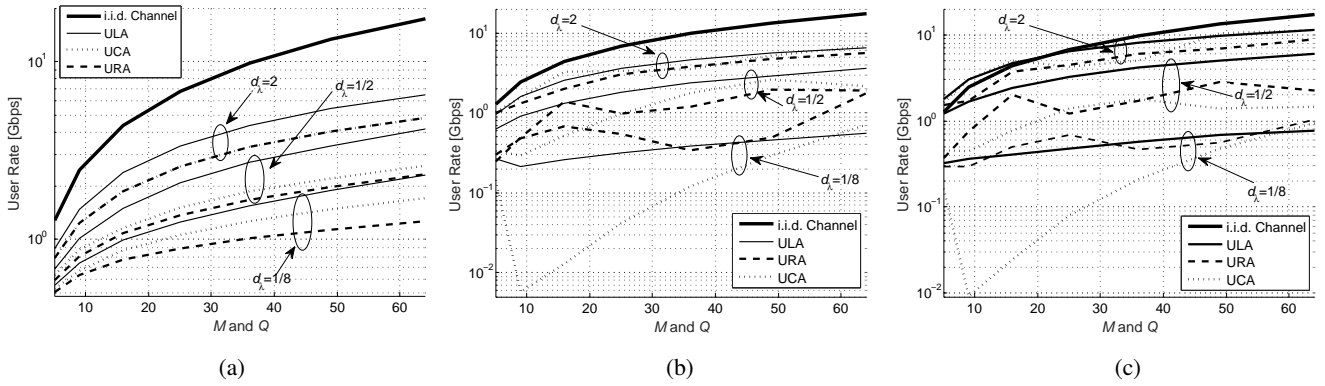

Fig. 14: User rate vs system size ($M = Q$) for various inter-element antenna spacings and antenna topologies. (a) Spatially correlated channel. (b) Spatially correlated channel with MC, $Z_L = 50\ \Omega$. (c) Spatially correlated channel with MC, $Z_L = 73 - j42.5\ \Omega$.

TABLE I: Simulation Parameters

Parameter	Numerical Value
Carrier frequency, f	28 GHz
Bandwidth, B	100 MHz
Antenna length, ι	$\lambda/2$
Antenna impedance, Z_A	$73 + 42.5j\ \Omega$
Received SNR, ρ	10 dB
Number of clusters, C	$\sim \max\left[\text{Poisson}(1.8), 1\right]$
Number of subpaths per clusters, L	20
Azimuth AOA and AOD central cluster angles, $\phi_{0,c}^{\text{AOA}}, \phi_{0,c}^{\text{AOD}}$	$\sim \mathcal{U}[0, 2\pi)\ \forall c$
Elevation AOA and AOD central cluster angles, $\theta_{0,c}^{\text{AOA}}, \theta_{0,c}^{\text{AOD}}$	LOS elevation angle
Azimuth AOA and AOD intra-cluster angular spread (°)	$\sim \text{Exp}(15.5)$ and $\sim \text{Exp}(10.2)$
Elevation AOA and AOD intra-cluster angular spread (°)	$\sim \text{Exp}(6.0)$ and $\sim \text{Exp}(3.9)$

elements as compared to the URA and UCA. Also, as shown in Table I, the small elevation RMS angular spreads, relative to the azimuth RMS angular spreads, limits the effectiveness of placing antenna elements with non-zero z-axis spacing. As a result, the URA and UCA performance is worse than the ULA, even for large inter-element antenna spacings, where the URA and UCA rates converge to similar values. When MC is modelled, there are large differences in the rates between different values of Z_L, particularly for the ULA. This observation is interesting since the results presented in Section V-A show that Z_L had minor impacts on the normalized SC, when MC is modelled. Previous works have shown that although the MC alters the SC structure, it also changes the effective gain of the antennas [30], [31], therefore varying the power in the resultant channel, $\overline{\mathbf{H}}$. The oscillatory nature of the rates, against inter-element spacing, when MC is added
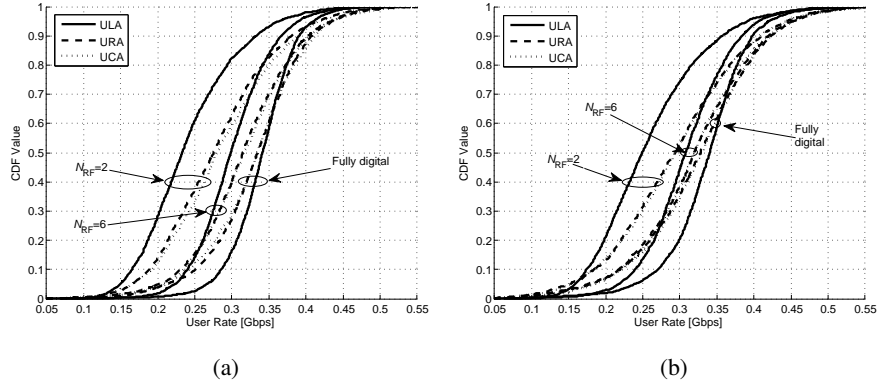
Fig. 15: User rate CDF of a 28 GHz mmWave channel for fully digital and HBF, where $M = 256$, $Q = 1$ and $d_\lambda = 1/2$. (a) Dipole antenna array. (b) X-pol antenna array.

suggests that the effective gain of the antennas is strongly related to the antenna inter-element spacing [30]. This is clearly seen by considering the UCA rate, which experiences the most channel power variation as the inter-element spacing is increased. For example, with $Z_L = 50 \ \Omega$, the UCA rate at an inter-element spacing of $d_\lambda \approx 0.43$ is more than 8 times the rate seen at a *larger* inter-element spacing of $d_\lambda \approx 0.6$.

To investigate the impacts of MC on the user rate by *only* variations in the effective SNR, i.e., no SC changes, we show the user rate as a function of inter-element spacing, d_λ, with a modified channel power in Figure 13c. The variation in effective SNR, with MC, can be shown to be $\alpha = \mathrm{tr}(\overline{\mathbf{H}}\overline{\mathbf{H}}^H)/\mathrm{tr}(\mathbf{H}\mathbf{H}^H)$, where $\overline{\mathbf{H}}$ is computed with $Z_L = 50 \ \Omega$. Thus, the user rate in Figure 13c, is given by

$$\text{User Rate} = B \log_2 \left| \mathbf{I}_Q + (\rho/M)\alpha\mathbf{H}\mathbf{H}^H \right|. \qquad (21)$$

Comparing Figures 13a and 13c, there are similar results for small inter-element spacings, where the power scaling effects are more noticeable, as discussed in Section V-B. As d_λ is increased, the effects of SC become more dominant and thus the two figures become dissimilar. The modified channel power user rate is more accurate for the ULA and emulates the effects of MC relatively well for inter-element spacings of up to $d_\lambda \approx 1$ wavelength. Considering the rates of the UCA, when a large increase in power is seen, the peaks in Figure 13a are reduced as compared with the peaks in Figure 13c. A possible reason for this might be that when MC increases the power, it also increases the SC, such that an overall gain is seen - but by not as much just the power increase.

2) Impact of Antenna Numbers: In Figure 14 we show the impact of system size on the user rate for various inter-element spacings and antenna topologies. When MC is not modelled, in Figure 14a, the UCA outperforms the URA for small inter-element spacings and becomes similar in performance to the URA as the inter-element spacing is increased. This trend was also seen in Figure 11 for the eigenvalue structure. The ULA has the largest rate for all inter-element spacings as it experiences less SC due to fewer adjacent antenna elements and more azimuth diversity. When MC is modelled, in Figures 14b and 14c, for $Z_L = 50 \ \Omega$ and $Z_L = 73 - j42.5 \ \Omega$,

respectively, the rates of the different antenna topologies are most affected at small inter-element spacings. For example, at $d_\lambda = 1/8$ and $M = Q = 9$, the UCA experiences a reduction in user rate of almost two orders of magnitude. This performance degradation of the UCA at small spacings was also seen in Figure 13 for $M = Q = 36$. As was the case in Figure 13, the ULA user rate for larger inter-element spacings is severely affected by Z_L, where the conjugate impedance matching increases the user rate significantly.

When MC is not included, the ULA topology consistently has the largest user rate due to both the sparse nature of the PES and the inherently smaller number of adjacent antenna elements. The effects of MC on normalized SC do not translate into similar trends for user rate due to the dominating effects of SNR variation. This effective antenna gain variation is strongly dependent on inter-element spacing and is seen to have more of an influence at smaller inter-element spacings.

D. User Rate with HBF

Figure 15 shows the user rate cumulative distribution function (CDF) for different antenna topologies with fully digital and HBF, where system parameters are given in Table I. This is shown for TX arrays of two different antennas types: dipole and x-pol [39], given in Figures 15a and 15b, respectively, where a x-pol antenna element consists of a $+45°$ and $-45°$ slant antenna. The inter-element spacing, d_λ, between the two antenna array types is kept constant such that the x-pol array is half the size of the dipole array. The x-pol ULA consists of 128 positions on the x-axis, while the URA and UCA are constructed with 16 x-pol positions on the x, y-plane and 8 x-pol positions in the direction of the z-axis. The HBF uses the OMP algorithm, as in [22], where the performance is shown for the number of RF chains, N_{RF}, equal to 2 and 6.

In the fully digital scenario the rate of the x-pol antenna array is slightly reduced compared to the dipole antenna array. This small decrease is a result of two factors: (i) the size of the TX antenna array is double in the dipole case for every topology and thus the probability of separating two propagation paths whose angles are similar is larger - due to its better spatial resolution, and (ii) the SC between two antenna elements forming a x-pol ($+45°$ and $-45°$) is non-zero [39].

Here in the fully digital case, the ULA has a larger median rate since the combined effect of all spatially correlated antennas is lower than the URA and UCA. Note that here the BF is done in both azimuth and elevation domains, whereas if the BF was only done in the elevation domain, one would expect the URA and UCA antenna topologies to outperform the ULA. Relative to the fully digital case, a large drop in sum rate is seen when HBF is used since N_{RF} is much less than M.

Interestingly, when HBF is used the ordering of the different antenna topologies rate CDFs is reversed, relative to the fully digital case. Also, for a given number of RF chains, N_{RF}, and antenna array topology, the x-pol antenna array has a better rate performance than the dipole case. Both of these observations can be explained by the poor behaviour of the OMP algorithm in channels with lower SC [22], and vice-versa.

VI. CONCLUSION

In this paper, we derive 3D SC closed-form expressions for wide, narrow and Von Mises PES. We define and derive diagonal dominance, a measure of massive MIMO convergence, for wide, narrow and Von Mises PES, while showing that the ULA converges much quicker than the URA and UCA topologies, due to the smaller numbers of adjacent antenna elements. Numerically, we then show the effects of MC on normalized SC, eigenvalue structure and user rate. MC is shown to decrease the normalized SC for side-by-side antennas at small inter-element spacings. However, the effects of MC on SC do not translate into similar trends in user rate, as the change in effective SNR from the MC becomes a dominating effect [30], and its variation is shown to be highly dependent on the antenna inter-element spacings. Here, the effects of MC on the user rate are more obvious at smaller inter-element spacings, agreeing with previous works [5], [29], [31], [56]. Also, the load impedance of the MC significantly affects the user rate of the ULA at larger inter-element spacings. HBF performance is then shown for dipole and x-pol antennas with the OMP algorithm, which is seen to work poorly for channels with low SC, such as those with the ULA. X-pol antenna arrays are shown to have a reduction in sum rate performance relative to dipole antenna arrays due to a smaller antenna array aperture size and non-zero x-pol SC. In every case, the poor HBF sum rate performance can be improved by increasing the number of RF chains.

APPENDIX A
PROOF OF LEMMA 1

Let $\mathbf{h}_m$ be the mth column of $\mathbf{H}$, then the SC between any two TX antenna elements $m, m' \in 1, \ldots, M$, with $\text{p}_{\Phi}(\phi_{c,l}^{\text{AOD}}) \sim \mathcal{U}[0, 2\pi] \ \forall c, l$, can be computed as [60]

$$R_{m,m'} = \mathbb{E}\left[\mathbf{h}_m^{\text{H}} \mathbf{h}_{m'}\right] \Big/ \sqrt{\mathbb{E}\left[\|\mathbf{h}_m^{\text{H}}\|^2\right] \mathbb{E}\left[\|\mathbf{h}_{m'}\|^2\right]}, \quad (22)$$

as all channels have zero mean, i.e., from (1), $\mathbb{E}[\mathbf{h}_m] = 0 \ \forall m$. Note that the expectation is taken over all small-scale fading: path gains and phases. Denoting $a_{\text{TX},m}(\phi_{c,l}^{\text{AOD}}, \theta_{c,l}^{\text{AOD}}t)$ as the

mth entry of $\mathbf{a}_{\text{TX}}(\phi_{c,l}^{\text{AOD}}, \theta_{c,l}^{\text{AOD}})$, the denominator can then be computed as

$$\mathbb{E}\left[\|\mathbf{h}_m^{\text{H}}\|^2\right] = \frac{1}{L} \sum_{c=1}^{C} \sum_{l=1}^{L} \mathbb{E}[\gamma_c] \mathbb{E}\left[\left|a_{\text{TX},m}(\phi_{c,l}^{\text{AOD}}, \theta_{c,l}^{\text{AOD}})\right|^2\right] \times$$
$$\left(\sum_{q=1}^{Q} \mathbb{E}\left[\left|a_{\text{RX},q}^{\text{H}}(\phi_{c,l}^{\text{AOA}}, \theta_{c,l}^{\text{AOA}})\right|^2\right]\right) = Q = \mathbb{E}\left[\|\mathbf{h}_{m'}\|^2\right] \quad (23)$$

since $\mathbb{E}[\gamma_c] = 1/C$ and each entry of $\mathbf{a}_{\text{RX}}(\phi_{c,l}^{\text{AOA}}, \theta_{c,l}^{\text{AOA}})$ and $\mathbf{a}_{\text{TX}}(\phi_{c,l}^{\text{AOD}}, \theta_{c,l}^{\text{AOD}})$ has unit norm. Likewise, the numerator of (22) can be calculated as,

$$\mathbb{E}\left[\mathbf{h}_m^{\text{H}} \mathbf{h}_{m'}\right] = \frac{1}{L} \sum_{c=1}^{C} \sum_{l=1}^{L} \mathbb{E}\left[\|\mathbf{a}_{\text{RX}}(\phi_{c,l}^{\text{AOA}}, \theta_{c,l}^{\text{AOA}})^{\text{H}}\|^2\right] \mathbb{E}\left[|g_{c,l}|^2\right]$$
$$\times \mathbb{E}\left[a_{\text{TX},m}(\phi_{c,l}^{\text{AOD}}, \theta_{c,l}^{\text{AOD}}) a_{\text{TX},m'}^*(\phi_{c,l}^{\text{AOD}}, \theta_{c,l}^{\text{AOD}})\right] \quad (24)$$
$$= \frac{Q}{CL} \sum_{c=1}^{C} \sum_{l=1}^{L} \mathbb{E}\left[a_{\text{TX},m}(\phi_{c,l}^{\text{AOD}}, \theta_{c,l}^{\text{AOD}}) a_{\text{TX},m'}^*(\phi_{c,l}^{\text{AOD}}, \theta_{c,l}^{\text{AOD}})\right]. \quad (25)$$

Combining (23) and (25), the SC in (22) can be written as

$$R_{m,m'} = \sum_{c=1}^{C} \sum_{l=1}^{L} \int_{\theta_{c,l}^{\text{AOD}}} \int_{\phi_{c,l}^{\text{AOD}}} \exp\left(j\frac{2\pi}{\lambda}(\mathbf{W}_{\text{TX},m} - \mathbf{W}_{\text{TX},m'}) \times\right.$$
$$\left. \mathbf{r}_{\text{TX}}(\phi_{c,l}^{\text{AOD}}, \theta_{c,l}^{\text{AOD}})\right) \frac{\text{f}_{\Phi}(\phi_{c,l}^{\text{AOD}}) \text{f}_{\Theta}(\theta_{c,l}^{\text{AOD}}) d\phi_{c,l}^{\text{AOD}} d\theta_{c,l}^{\text{AOD}}}{CL} \quad (26)$$
$$= \frac{1}{CL} \sum_{c=1}^{C} \sum_{l=1}^{L} \int_{\theta_{c,l}^{\text{AOD}}} \int_{\phi_{c,l}^{\text{AOD}}} \exp\left(j2\pi\left[dx_{m,m'} \sin(\theta_{c,l}^{\text{AOD}}) \times \right.\right.$$
$$\cos(\phi_{c,l}^{\text{AOD}}) + dy_{m,m'} \sin(\theta_{c,l}^{\text{AOD}}) \sin(\phi_{c,l}^{\text{AOD}}) + dz_{m,m'} \quad (27)$$
$$\times \cos(\theta_{c,l}^{\text{AOD}})\big]\big) \, \text{p}_{\Phi}(\phi_{c,l}^{\text{AOD}}) \text{p}_{\Theta}(\theta_{c,l}^{\text{AOD}}) \sin(\theta_{c,l}^{\text{AOD}}) d\phi_{c,l}^{\text{AOD}} d\theta_{c,l}^{\text{AOD}}$$
$$= \frac{1}{CL} \sum_{c=1}^{C} \sum_{l=1}^{L} \int_{\theta_{c,l}^{\text{AOD}}} \left(\int_{\phi_{c,l}^{\text{AOD}}} \exp\left(j2\pi \sin(\theta_{c,l}^{\text{AOD}}) [dx_{m,m'}\right.\right.$$
$$\left.\times \cos(\phi_{c,l}^{\text{AOD}}) + dy_{m,m'} \sin(\phi_{c,l}^{\text{AOD}})]\right) \text{p}_{\Phi}(\phi_{c,l}^{\text{AOD}}) d\phi_{c,l}^{\text{AOD}}\right)$$
$$\exp\left(j2\pi dz_{m,m'} \cos(\theta_{c,l}^{\text{AOD}})\right) \text{p}_{\Theta}(\theta_{c,l}^{\text{AOD}}) \sin(\theta_{c,l}^{\text{AOD}}) d\theta_{c,l}^{\text{AOD}}, (28)$$

where $\mathbf{W}_{\text{TX},m}$ denotes the mth row of $\mathbf{W}_{\text{TX}}$, while $dx_{m,m'} = dx_m - dx_{m'}$, $dy_{m,m'} = dy_m - dy_{m'}$ and $dz_{m,m'} = dz_m - dz_{m'}$ denote the distances between antenna element m and m' in wavelengths relative to the x, y and z axes, respectively. Evaluating the integral in (28) with respect to $\phi_{c,l}^{\text{AOD}}$, we have

$$\int_{\phi_{c,l}^{\text{AOD}}} \exp\left(j2\pi \sin(\theta_{c,l}^{\text{AOD}}) \left[dx_{m,m'} \cos\left(\phi_{c,l}^{\text{AOD}}\right) + dy_{m,m'}\right.\right.$$
$$\left.\times \sin(\phi_{c,l}^{\text{AOD}})\right]) \, \text{p}(\phi_{c,l}^{\text{AOD}}) d\phi_{c,l}^{\text{AOD}} = \frac{1}{2\pi} \int_0^{2\pi} \exp\left(\sin(\theta_{c,l}^{\text{AOD}})\right.$$
$$\left.\times j2\pi \sqrt{dx_{m,m'}^2 + dy_{m,m'}^2} \cos(\phi_{c,l}^{\text{AOD}} + \varphi)\right) d\phi_{c,l}^{\text{AOD}} \quad (29)$$
$$= \int_0^{2\pi} \frac{\exp\left(j2\pi \sin(\theta_{c,l}^{\text{AOD}}) dxy_{m,m'} \cos(\phi_{c,l}^{\text{AOD}})\right)}{2\pi} d\phi_{c,l}^{\text{AOD}} \quad (30)$$
$$= J_0\left(2\pi \sin(\theta_{c,l}^{\text{AOD}}) dxy_{m,m'}\right), \quad (31)$$

where the phase offset in (29), $\varphi = \text{atan2}(dx_{m,m'}, dy_{m,m'}) + \frac{\pi}{2}$, has no effect because the integration is taken over a whole period, and the integral in (30) is evaluated in [61] pp. 491. $dxy_{m,m'} = \sqrt{dx_{m,m'}^2 + dy_{m,m'}^2}$ is the distance in wavelengths between antenna element m and m' on the x, y-plane. Substituting (31) in (28) gives the desired result.

APPENDIX B
PROOF OF THEOREM 1

For any two antenna elements n and n', where $\theta \in [0, \pi)$ is an arbitrary elevation angle and $\text{p}_\Theta(\theta)$ is constant over $[0, \pi)$, we have

$$\int_\theta \exp\left(j2\pi dz_{n,n'} \cos(\theta)\right) J_0\left(2\pi dxy_{n,n'} \sin(\theta)\right) \text{p}_\Theta(\theta)$$
$$\times \sin(\theta)\, d\theta = A \int_0^\pi \exp\left(j2\pi dz_{n,n'} \cos(\theta)\right)$$
$$\times J_0\left(2\pi dxy_{n,n'} \sin(\theta)\right) \text{p}_\Theta(\theta) \sin(\theta)\, d\theta, \quad (32)$$

where A is the scaling constant to make sure the elevation PDF integrates to 1. To calculate A, we have $1 = A \int_\theta \text{p}_\Theta(\theta) \sin(\theta) d\theta = A \int_0^\pi \sin(\theta) d\theta = 2A$, therefore $A = 1/2$. Substituting $u = -\cos(\theta)$, from (32) we have

$$R_{m,m'} = \int_{-1}^1 \frac{\exp(-j2\pi dz_{n,n'} u)}{2\sin(\theta)} J_0\left(2\pi dxy_{n,n'} \sqrt{1-u^2}\right)$$
$$\times \sin(\theta) du \quad (33)$$

$$= \frac{1}{2} \int_{-1}^1 \exp(-j2\pi dz_{n,n'} u) I_0\left(j2\pi dxy_{n,n'} \sqrt{1-u^2}\right) du \quad (34)$$

$$= \frac{\sinh\left(\sqrt{(j2\pi dz_{n,n'})^2 + (j2\pi dxy_{n,n'})^2}\right)}{\sqrt{(j2\pi dz_{n,n'})^2 + (j2\pi dxy_{n,n'})^2}} \quad (35)$$

$$= \text{sinc}\left(2dxyz_{n,n'}\right), \quad (36)$$

where the evaluated integral, in (34), is given in [61] pp. 698.

APPENDIX C
PROOF OF THEOREM 2

By using a narrow AOD PES, $\text{p}_\Theta(\theta_{c,l}^{\text{AOD}})$, distributed uniformly between $\theta_0^{\text{AOD}} - \Delta\theta_{c,l}^{\text{AOD}}$ and $\theta_0^{\text{AOD}} + \Delta\theta_{c,l}^{\text{AOD}} \; \forall c, l$, where $\Delta\theta_{c,l}^{\text{AOD}}$ is small, we can approximate the integral in (6) by its range multiplied by the central value. To make sure that the elevation PDF integrates to 1, we have $1 = A \int_{\theta_0^{\text{AOD}} - \Delta\theta_{c,l}^{\text{AOD}}}^{\theta_0^{\text{AOD}} + \Delta\theta_{c,l}^{\text{AOD}}} \sin(\theta_{c,l}^{\text{AOD}}) d\theta_{c,l}^{\text{AOD}} \approx 2A\Delta\theta_{c,l}^{\text{AOD}} \sin(\theta_0^{\text{AOD}})$. Therefore $A \approx 1/(2\Delta\theta_{c,l}^{\text{AOD}} \sin(\theta_0^{\text{AOD}}))$. From (6), we have

$$R_{n,n'} \approx \frac{1}{CL} \sum_{c=1}^C \sum_{l=1}^L \frac{1}{2\Delta\theta_{c,l}^{\text{AOD}} \sin(\theta_0^{\text{AOD}})}$$
$$\times \int_{\theta_0^{\text{AOD}} - \Delta\theta_{c,l}^{\text{AOD}}}^{\theta_0^{\text{AOD}} + \Delta\theta_{c,l}^{\text{AOD}}} \exp\left(j2\pi dz_{m,m'} \cos(\theta_{c,l}^{\text{AOD}})\right)$$
$$\times J_0\left(2\pi dxy_{m,m'} \sin(\theta_{c,l}^{\text{AOD}})\right) \sin(\theta_{c,l}^{\text{AOD}}) d\theta_{c,l}^{\text{AOD}} \quad (37)$$
$$= \frac{1}{CL} \sum_{c=1}^C \sum_{l=1}^L \exp\left(j2\pi dz_{m,m'} \cos(\theta_0^{\text{AOD}})\right)$$

$$\times J_0\left(2\pi dxy_{m,m'} \sin(\theta_0^{\text{AOD}})\right) \quad (38)$$
$$= \exp\left(j2\pi dz_{m,m'} \cos(\theta_0^{\text{AOD}})\right) J_0\left(2\pi dxy_{m,m'} \sin(\theta_0^{\text{AOD}})\right). \quad (39)$$

APPENDIX D
PROOF OF THEOREM 3

For any two antenna elements n and n', where $\theta \in [0, \pi)$ is an arbitrary elevation angle, and $\text{p}_\Theta(\theta) \sim \exp\left(\kappa \cos(\theta - \mu)\right)/2\pi I_0(\kappa)$, the SC in (6) can be approximated as

$$R_{n,n'} = \frac{A}{2\pi I_0(\kappa)} \int_0^\pi \exp\left(j2\pi dz_{n,n'} \cos(\theta)\right) \times$$
$$J_0\left(2\pi dxy_{n,n'} \sin(\theta)\right) \sin(\theta) \exp(\kappa \cos(\theta - \mu)) d\theta \quad (40)$$
$$\approx \frac{A}{2\pi I_0(\kappa)} \exp(\kappa \sin(\mu)) \int_0^\pi \exp\left(j2\pi dz_{n,n'} \cos(\theta)\right) \sin(\theta)$$
$$\times J_0\left(2\pi dxy_{n,n'}\right) \sin(\theta) \exp(\kappa \cos(\mu) \cos(\theta)) d\theta, \quad (41)$$

where A is the scaling constant to make sure the elevation PDF integrates to unity and we approximate $\kappa \sin(\mu) \sin(\theta) \approx \kappa \sin(\mu)$, assuming that $\theta \approx \pi/2$. This approximation is best for $\mu = \pi/2$, but is reasonable accurate for a wide range of μ values. To calculate A, we have

$$1 = \frac{A \exp(\kappa \sin(\mu))}{2\pi I_0(\kappa)} \int_0^\pi \sin(\theta) \exp(\kappa \cos(\mu) \cos(\theta)) d\theta \quad (42)$$

$$= \frac{A \exp(\kappa \sin(\mu))}{2\pi I_0(\kappa)} \int_{-1}^1 \exp(-\kappa \cos(\mu) u) du \quad (43)$$

$$= \frac{A \exp(\kappa \sin(\mu))}{2\pi \kappa \cos(\mu) I_0(\kappa)} \left[\exp(\kappa \cos(\mu)) - \exp(-\kappa \cos(\mu))\right] \quad (44)$$
$$= A \exp(\kappa \sin(\mu)) \sinh(\kappa \cos(\mu))/\pi \kappa \cos(\mu) I_0(\kappa) \quad (45)$$

where $u = -\cos(\theta)$ is substituted in (43). Therefore $A = \pi\kappa \cos(\mu) I_0(\kappa)/\exp(\kappa \sin(\mu)) \sinh(\kappa \cos(\mu))$. Denoting $B = 2\pi dxy_{n,n'}$, $D = \kappa \cos(\mu)/j$, $E = 2\pi dz_{n,n'}$ and substituting $v = -\cos(\theta)$ the integral in (41) can be evaluated as

$$\int_{-1}^1 J_0\left(B\sqrt{1-v^2}\right) [\cos(Ev) + j\sin(Ev)] [\cos(Dv)$$
$$+ j\sin(Dv)]\, dv = \int_{-1}^1 J_0\left(B\sqrt{1-v^2}\right) \cos((E+D)v) dv$$
$$+ j\int_{-1}^1 J_0\left(B\sqrt{1-v^2}\right) \sin((E+D)v) dv \quad (46)$$
$$= 2\sin(\sqrt{B^2 + (E+D)^2})/\sqrt{B^2 + (E+D)^2}, \quad (47)$$

where the second term in (46) integrates to zero. Thus, substituting (47) and the normalization constant, A, into (41), we obtain the desired result.

APPENDIX E
PROOF OF LEMMA 2

If $\mathbf{h}_q$ denotes the qth row of $\mathbf{H}$, for $q, q' \in 1, \ldots, Q$,

$$\mathbb{E}\left[\mathbf{h}_q \mathbf{h}_{q'}^{\text{H}}\right] = \sum_{c=1}^C \sum_{l=1}^L \int_{\theta_{c,l}^{\text{AOA}}} \int_{\phi_{c,l}^{\text{AOA}}} \exp\left(j(\mathbf{W}_{\text{RX},q} - \mathbf{W}_{\text{RX},q'})\right.$$
$$\left. \times \frac{2\pi}{\lambda} \mathbf{r}_{\text{RX}}(\phi_{c,l}^{\text{AOA}}, \theta_{c,l}^{\text{AOA}})\right) \sin(\theta_{c,l}^{\text{AOA}}) \text{p}_\Phi(\phi_{c,l}^{\text{AOA}}) \text{p}_\Theta(\theta_{c,l}^{\text{AOA}})$$

$$\times \frac{M}{CL} d\phi_{c,l}^{\text{AOA}} d\theta_{c,l}^{\text{AOA}} \quad (48)$$

$$= \frac{M}{CL} \sum_{c=1}^{C} \sum_{l=1}^{L} \int_{\theta_{c,l}^{\text{AOA}}} \exp\left(j2\pi dz_{q,q'} \cos(\theta_{c,l}^{\text{AOA}})\right) \sin(\theta_{c,l}^{\text{AOA}})$$

$$\times J_0\left(2\pi dxy_{q,q'} \sin(\theta_{c,l}^{\text{AOA}})\right) \text{p}_\Theta(\theta_{c,l}^{\text{AOA}}) d\theta_{c,l}^{\text{AOA}} \quad (49)$$

$$= \frac{M}{CL} \sum_{c=1}^{C} \sum_{l=1}^{L} \mathbb{E}\left[\exp\left(j2\pi dz_{q,q'} \cos(\theta_{c,l}^{\text{AOA}})\right)\right.$$

$$\left. \times J_0\left(2\pi dxy_{q,q'} \sin(\theta_{c,l}^{\text{AOA}})\right)\right], \quad (50)$$

where steps from (48) to (49) are given in Appendix A with $\text{p}_\Phi(\phi_{c,l}^{\text{AOA}}) \sim \mathcal{U}[0, 2\pi) \; \forall c, l$.

REFERENCES

[1] "ITU Radiocommunication Study Groups, 27th meeting of Working Party 5D, Niagra Falls, Canada, Document: 5D/TEMP/371-E: WG Spectrum Aspects," June 2017.

[2] M. Shafi, *et al.*, "5G: A tutorial overview of standards, trials, challenges, deployment, and practice," *IEEE J. Sel. Areas Commun.*, vol. 35, no. 6, pp. 1201–1221, June 2017.

[3] T. S. Rappaport, *et al.*, "Millimeter wave mobile communications for 5G cellular: It will work!" *IEEE Access*, vol. 1, pp. 335–349, May 2013.

[4] D. López-Pérez, *et al.*, "Towards 1Gbps/UE in cellular systems: Understanding ultra-dense small cell deployments," *IEEE Commun. Surveys. Tuts.*, vol. 17, no. 4, pp. 2078–2101, June 2015.

[5] F. Rusek, *et al.*, "Scaling up MIMO: Opportunities and challenges with very large arrays," *IEEE Signal Process. Mag.*, vol. 30, no. 1, pp. 40–60, January 2013.

[6] W. Roh, *et al.*, "Millimeter-wave beamforming as an enabling technology for 5G cellular communications: Theoretical feasibility and prototype results," *IEEE Commun. Mag.*, vol. 52, no. 2, pp. 106–113, February 2014.

[7] S. Rangan, *et al.*, "Millimeter-wave cellular wireless networks: Potentials and challenges," *Proceedings of the IEEE*, vol. 102, no. 3, pp. 366–385, February 2014.

[8] M. R. Akdeniz, *et al.*, "Millimeter wave channel modeling and cellular capacity evaluation," *IEEE J. Sel. Areas Commun.*, vol. 32, no. 6, pp. 1164–1179, June 2014.

[9] S. Hur, *et al.*, "Proposal on millimeter-wave channel modeling for 5G cellular system," *IEEE J. Sel. Topics Signal Process.*, vol. 10, no. 3, pp. 454–469, February 2016.

[10] T. S. Rappaport, *et al.*, "Wideband millimeter-wave propagation measurements and channel models for future wireless communication system design," *IEEE Trans. Commun.*, vol. 63, no. 9, pp. 3029–3056, September 2015.

[11] ——, "Broadband millimeter-wave propagation measurements and models using adaptive-beam antennas for outdoor urban cellular communications," *IEEE Trans. Antennas and Propag.*, vol. 61, no. 4, pp. 1850–1859, December 2012.

[12] M. K. Samimi, *et al.*, "3-D statistical channel model for millimeter-wave outdoor mobile broadband communications," *IEEE Intl. Conf. Commun.*, pp. 2430–2436, June 2015.

[13] A. L. Swindlehurst, *et al.*, "Millimeter-wave massive MIMO: The next wireless revolution?" *IEEE Commun. Mag.*, vol. 52, no. 9, pp. 56–62, September 2014.

[14] T. A. Thomas, *et al.*, "3D mmWave channel model proposal," *IEEE Veh. Technol. Conf.*, pp. 1–6, September 2014.

[15] T. S. Rappaport, *et al.*, "Investigation and comparison of 3GPP and NYUSIM channel models for 5G wireless communications," *IEEE Veh. Technol. Conf.*, September 2017.

[16] W. C. Jakes, *Microwave Mobile Communications*. New York: Wiley, 1974.

[17] C. Masouros, *et al.*, "Large-scale MIMO transmitters in fixed physical spaces: The effect of transmit correlation and mutual coupling," *IEEE Trans. Commun.*, vol. 61, no. 7, pp. 2794–2804, July 2013.

[18] C. T. Neil, *et al.*, "On the impact of antenna topologies for massive MIMO systems," *IEEE Intl. Conf. Commun.*, pp. 2030–2035, June 2015.

[19] J. Salz, *et al.*, "Effect of fading correlation on adaptive arrays in digital mobile radio," *IEEE Trans. Veh. Technol.*, vol. 43, no. 4, pp. 1049–1057, November 1994.

[20] D-S. Shiu, *et al.*, "Fading correlation and its effect on the capacity of multielement antenna systems," *IEEE Trans. Commun.*, vol. 48, no. 3, pp. 502–513, March 2000.

[21] A. M. Tulino, *et al.*, "Impact of antenna correlation on the capacity of multiantenna channels," *IEEE Trans. Inf. Theory*, vol. 51, no. 7, pp. 2491–2509, July 2005.

[22] O. El Ayach, *et al.*, "Spatially sparse precoding in millimeter wave MIMO systems," *IEEE Trans. Wireless Commun.*, vol. 13, no. 3, pp. 1499–1513, March 2014.

[23] J. Brady, *et al.*, "Beamspace MIMO for millimeter-wave communications: System architecture, modeling, analysis, and measurements," *IEEE Trans. Antennas Propag.*, vol. 61, no. 7, pp. 3814–3827, July 2013.

[24] A. Forenza, *et al.*, "Simplified spatial correlation models for clustered MIMO channels with different array configurations," *IEEE Trans. Veh. Technol.*, vol. 56, no. 4, pp. 1924–1934, July 2007.

[25] Y. F. Alem, *et al.*, "3D spatial fading correlation for uniform angle of arrival distribution," *IEEE Commun. Lett.*, vol. 19, no. 6, pp. 1073–1076, June 2015.

[26] Q-U-A. Nadeem, *et al.*, "A generalized spatial correlation model for 3D MIMO channels based on the Fourier coefficient of power spectrums," *IEEE Trans. Signal Process.*, vol. 63, no. 14, pp. 3671–3686, July 2015.

[27] S. K. Yong, *et al.*, "Three-dimensional spatial fading correlation models for compact MIMO receivers," *IEEE Trans. Wireless Commun.*, vol. 4, no. 6, pp. 2856–2869, November 2005.

[28] B. Clerckx, *et al.*, "Impact of antenna coupling on 2x2 MIMO communications," *IEEE Trans. Veh. Technol.*, vol. 56, no. 3, pp. 1009–1018, May 2007.

[29] J. W. Wallace, *et al.*, "Mutual coupling in MIMO wireless systems: A rigorous network theory analysis," *IEEE Trans. Wireless Commun.*, vol. 3, no. 4, pp. 1317–1325, July 2004.

[30] M. K. Özdemir, *et al.*, "Dynamics of spatial correlation and implications on MIMO systems," *IEEE Commun. Mag.*, vol. 42, no. 6, pp. S14–S19, June 2004.

[31] R. Janaswamy, "Effect of element mutual coupling on the capacity of fixed length linear arrays," *IEEE Antennas Wireless Propag. Lett.*, vol. 1, no. 1, pp. 157–160, 2002.

[32] S. Biswas, *et al.*, "Performance analysis of large multiuser MIMO systems with space-contrained 2-D antenna arrays," *IEEE Trans. Wireless Commun.*, vol. 15, no. 5, pp. 3492–3505, January 2016.

[33] A. A. M. Saleh, *et al.*, "A statistical model for indoor multipath propagation," *IEEE J. Sel. Areas Commun.*, vol. 5, no. 2, pp. 128–137, February 1987.

[34] J. G. Andrews, *et al.*, "Modeling and analyzing millimeter wave cellular systems," *IEEE Trans. Commun.*, vol. 65, no. 1, pp. 403–430, January 2017.

[35] B. Mondal, *et al.*, "3D channel model in 3GPP," *IEEE Communications Magazine*, vol. 53, no. 3, pp. 16–23, March 2015.

[36] A. F. Molisch, *et al.*, "Capacity of MIMO systems based on measured wireless channels," *IEEE J. Sel. Areas Commun.*, vol. 20, no. 3, pp. 561–569, April 2002.

[37] J. W. Wallace, *et al.*, "Modeling the indoor MIMO wireless channel," *IEEE Trans. Antennas and Propag.*, vol. 50, no. 5, pp. 591–599, May 2002.

[38] ——, "Power and complex envelope correlation for modeling measured indoor MIMO channels: A beamforming evaluation," *IEEE Veh. Technol. Conf.*, October 2003.

[39] "3GPP TR 36.873 V12.2.0 Technical Report: Study on 3D channel model for LTE (release 12)," June 2015, available: http://www.3gpp.org/.

[40] "3GPP TR 38.900 V14.0.0 Technical Report: Study on channel model for frequency spectrum above 6 GHz (release 14)," June 2016.

[41] M. K. Samimi, *et al.*, "Ultra-wideband statistical channel model for non line of sight millimeter-wave urban channels," *IEEE Global Commun. Conf.*, pp. 3483–3489, December 2014.

[42] ——, "Local multipath model parameters for generating 5G millimeter-wave 3GPP-like channel impulse response," *IEEE European Conf. Antennas Propag.*, April 2016.

[43] A. Alkhateeb, *et al.*, "Channel estimation and hybrid precoding for millimeter wave cellular systems," *IEEE J. Sel. Topics Signal Process.*, vol. 8, no. 5, pp. 831–846, October 2014.

[44] R. W. Heath Jr., *et al.*, "An overview of signal processing techniques for millimeter wave MIMO systems," *IEEE J. Sel. Topics Signal Process.*, vol. 10, no. 3, pp. 436–453, April 2016.

[45] K. Haneda, *et al.*, "Measurement-based analysis of spatial degrees of freedom in multipath propagation channels," *IEEE Trans. Antennas Propag.*, vol. 61, no. 2, pp. 890–900, February 2013.

[46] J. Zhang, *et al.*, "Three-dimensional fading channel models: A survey of elevation angle research," *IEEE Commun. Mag.*, vol. 52, no. 6, pp. 218–226, June 2014.

[47] M. Shafi, *et al.*, "Polarized MIMO channels in 3-D: Models, measurements and mutual information," *IEEE J. Sel. Areas Commun.*, vol. 24, no. 3, pp. 514–527, 2006.

[48] H. Q. Ngo, *et al.*, "Energy and spectral efficiency of very large multiuser MIMO systems," *IEEE Trans. Commun.*, vol. 61, no. 4, pp. 1436–1449, April 2013.

[49] P. J. Smith, *et al.*, "On the convergence of massive MIMO systems," *IEEE Intl. Conf. Commun.*, pp. 5191–5196, June 2014.

[50] G. R. MacCartney Jr., *et al.*, "Omnidirectional path loss models in New York City at 28 GHz and 73 GHz," *IEEE Intl. Symp. Pers. Indoor Mobile Radio Commun.*, pp. 227–231, September 2014.

[51] M. A. Sedaghat, *et al.*, "Load modulated arrays: A low-complexity antenna," *IEEE Commun. Mag.*, vol. 54, no. 3, pp. 46–52, March 2016.

[52] M. T. Ivrlač, *et al.*, "Toward a circuit theory of communication," *IEEE Trans. Circuits Syst. I, Reg. Papers*, vol. 57, no. 7, pp. 1663–1683, July 2010.

[53] C. A. Balanis, *Antenna Theory: Analysis and Design*, 3rd ed. John Wiley and Sons, 2005.

[54] Y. Wu, *et al.*, "Effects of antenna mutual coupling on the performance of MIMO systems," *Symp. Inf. Theory*, 2008.

[55] P. N. Fletcher, *et al.*, "Mutual coupling in multi-element array antennas and its influence on MIMO channel capacity," *IET Electron. Lett.*, vol. 39, no. 4, pp. 342–344, February 2003.

[56] B. K. Lau, *et al.*, "Capacity analysis for compact MIMO systems," *IEEE Veh. Technol. Conf.*, vol. 1, pp. 165–170, May 2005.

[57] A. S. Y. Poon, *et al.*, "Degrees of freedom in multiple-antenna channels: A signal space approach," *IEEE Trans. Inf. Theory*, vol. 51, no. 2, pp. 523–536, February 2005.

[58] S. Sun, *et al.*, "MIMO for millimeter-wave wireless communications: Beamforming, spatial multiplexing, or both?" *IEEE Commun. Mag.*, vol. 52, no. 12, pp. 110–121, December 2014.

[59] G. J. Foschini, *et al.*, "On limits of wireless communications in a fading environment when using multiple antennas," *Wireless Pers. Commun.*, vol. 6, no. 3, pp. 311–335, March 1998.

[60] R. J. Muirhead, *Aspects of Multivariate Statistical Theory*, 2nd ed. Wiley, 2005.

[61] I. S. Gradshteyn, *et al.*, *Table of Integrals, Series, and Products*, 7th ed. Elsevier Inc., 2007.